Physics – Uspekhi **67** (3) 293 – 313 (2024)

CONFERENCES AND SYMPOSIA

PACS numbers: **42.55. – f, 52.30. – q, 52.38. – r**, 52.38.Kd

ON THE 100th ANNIVERSARY OF THE BIRTH OF N G BASOV

Research in plasma physics and particle acceleration using the PEARL petawatt laser

A A Soloviev, K F Burdonov, V N Ginzburg, M Yu Glyavin, R S Zemskov, A V Kotov, A A Kochetkov, A A Kuzmin, A A Murzanev, I B Mukhin, S E Perevalov, S A Pikuz, M V Starodubtsev, A N Stepanov, J Fuchs, I A Shaykin, A A Shaykin, I V Yakovlev, E A Khazanov

DOI: https://doi.org/10.3367/UFNe.2022.11.039612

Contents

Abstract. The PEARL laser-plasma complex is set up on the basis of a petawatt laser and allows a wide range of experiments in laser-plasma interactions, including particle acceleration, X-ray generation, and research in the area of high energy density physics. Constant work to improve the system makes it possible not only to systematically expand experimental capabilities but also to develop new technologies for megascience class facilities. The paper outlines possible experimental scenarios for using the laser and provides a description of experiments already carried out with the laser in a broad range of areas.

Keywords: petawatt lasers, laser plasma, laser particle acceleration, laboratory astrophysics

A A Soloviev [(1,*)], **K F Burdonov** [(1)], **V N Ginzburg** [(1)], **M Yu Glyavin** [(1)], **R S Zemskov** [(1)], **A V Kotov** [(1)], **A A Kochetkov** [(1)], **A A Kuzmin** [(1)], **A A Murzanev** [(1)], **I B Mukhin** [(1)], **S E Perevalov** [(1)], **S A Pikuz** [(2)], **M V Starodubtsev** [(1)], **A N Stepanov** [(1)], **J Fuchs** [(3)], **I A Shaykin** [(1)], **A A Shaykin** [(1)], **I V Yakovlev** [(1)], **E A Khazanov** [(1)]

[(1)] A V Gaponov-Grekhov Institute of Applied Physics, Russian Academy of Sciences, ul. Ulyanova 46, 603950 Nizhny Novgorod, Russian Federation

[(2)] Joint Institute for High Temperatures, Russian Academy of Sciences, ul. Izhorskaya 13, str. 2, 125412 Moscow, Russian Federation

[(3)] École polytechnique, 91128 Palaiseau, France

E-mail: [(*)] so_lo@ipfran.ru

Received 20 November 2023
Uspekhi Fizicheskikh Nauk **194** (3) 313 – 335 (2024)
Translated by E N Ragozin

1. Introduction

The PEARL laser facility was developed at the Institute of Applied Physics RAS in 2007 [1] based on optical parametric chirped pulse amplification (OPCPA) technology. The laser radiation relied on the synchronization technologies which were unique at that time [2], a nanosecond neodymium-glass laser amplifier (300 J, 1 ns) [3], and the technology for manufacturing large-aperture DKDP crystals [4]. At that time, the laser became the most powerful parametric system in the world, and even now, almost two decades later, it remains a popular scientific instrument for conducting, first and foremost, basic scientific research. The technologies employed largely determined both the laser parameters and the applied significance of the laser complex.

The technology of parametric amplification of chirped pulses has proven itself, primarily due to its exceptional experimental parameters. First, there is absolutely no prepulse in the system outside the time window of the pump pulse, which results in a relatively low prepulse energy and intensity without additional effort aimed at improving the contrast ratio. Second, at operating repetition rates, there are virtually no thermal effects in parametric crystals, which greatly simplifies wavefront correction for optimal focusing and achieving maximum intensity. Third, the laser system is relatively tolerant to back reflections because there is no gain on backward propagation through the active element. Furthermore, in the initial configuration [1], there occurred a parametric frequency conversion (transition from signal to idler wave) at the first stage of parametric amplification, as a

result of which the parametric amplifier acted as an optical isolator, so the back reflection could not reach the front end in principle. All these features made it is possible to obtain record efficiency of interaction of femtosecond laser radiation with matter, in the interaction with both gas and solid targets [5–7], and the results are in good agreement with similar studies at other laser facilities around the world with similar laser parameters [8–11].

At the same time, a distinctive feature of parametric amplification is the strict requirements for the synchronization between the signal and the pump pulses. To meet these requirements, the problem of electrical synchronization of signal and pump pulses [2] from two different master oscillators, one based on Q-switching and the other on mode locking, was solved already at the design stage of the laser facility. Recently, the PEARL system underwent additional upgrades [12, 13], with the result that the relatively small jitter of the order of 50 ps [2] between the signal and the pump was further reduced to sub-picosecond values by switching to optical synchronization between the signal and the pump pulses.

However, the technological difficulties overcome at the design stage became the key advantage of the laser system at the stage of applied research in laboratory astrophysics. The high precision synchronization of the nanosecond laser driver and femtosecond radiation allow pump-probe experiments with a probe pulse of exceptional optical quality, enabling for clear interferometric shadow and polarization images, as well as the most accurate investigation of time dynamics due to low jitter. To implement the pump-probe technique, an original scheme for extracting a nanosecond pulse from the pump laser was developed [14], which makes it possible to have a nanosecond pulse with an energy of up to 250 J perfectly synchronized with the signal without energy loss of the femtosecond pulse. In concert with the original pulsed magnetic system [15], the facility offers a unique combination of conditions for scaled modeling of plasma astrophysical processes like matter accretion [16], jet collimation [17], and the experimental study of magnetohydrodynamic [18] and kinetic instabilities [19] in plasmas.

The technologies employed in the laser system have proven themselves well and laid the basis for the XCELS exawatt project [20, 21]. The recently emerged CafCA technology for increasing the peak power [22], together with the approaches developed for wavefront correction [23, 24], in particular of nonlinear phase distortions [25], have made it possible not only to significantly increase the power of the laser system [26] but also to almost proportionally increase the peak focal intensity [27], which further expanded the range of possible laser parameters on the target towards higher intensities. The use of CafCA technology for a probing pulse, among other things, makes it possible to increase, when necessary, the time resolution of optical diagnostics of relativistic objects, for example, to study the BISER radiating singularity [28].

The review outlines the experimental research pursued at the PEARL facility. Section 2 describes in detail the experimental capabilities of the facility, including laser parameters and the feasibility of conducting experiments and implementing diagnostic methods. Descriptions of the experiments performed are grouped in Sections 3 and 4. Section 3 presents experiments on laser plasma acceleration of electrons (Section 3.1) and protons (Section 3.2); Section 3.3 contains experiments with secondary radiation obtained during laser-plasma interaction. Section 4 summarizes experiments on laboratory modeling of astrophysical phenomena. Section 5 briefly describes future prospects and plans for research on PEARL.

2. Experimental capabilities of the complex

2.1 Description of the facility, schematic diagram of the laser, laser parameters

The PEARL laser complex is a parametric laser system with chirped pulse amplification, a schematic diagram of which is shown in Fig. 1.

Table 1 shows the approximate parameters of the main operating modes of the PEARL laser after the upgrade. The limiting pulse duration in single-pulse and pulse-periodic (frequency) modes is indicated without taking into account the use of CafCA technology and may be slightly longer due to nonperfect compressor alignment. The pulse-periodic mode differs from the single-pulse mode in that there is no pumping in the last parametric amplification stage, which allows operation at a higher repetition rate. In the nanosecond mode, pump radiation is used, which can be extracted at one of the stages of its amplification. The nanosecond mode can be used in conjunction with both the single-pulse and pulse-periodic modes, and separately.

In the single-pulse mode, the energy at the compressor output can exceed 20 J and is limited by the radiation resistance of the diffraction gratings. The pulse aperture at the compressor output, depending on the setting, ranges from 160 to 180 mm. The duration is about 30 fs (given are the actual parameters reached after the upgrade, including the transition to a front-end system with optical synchronization [13]). The central wavelength is 910 nm. The spectral width is limited by the compressor bandwidth, which is ~ 100 nm. The architecture of the laser system implies the presence of nanosecond pump radiation at a wavelength of 1054 nm, with an energy of more than 250 J at the fundamental

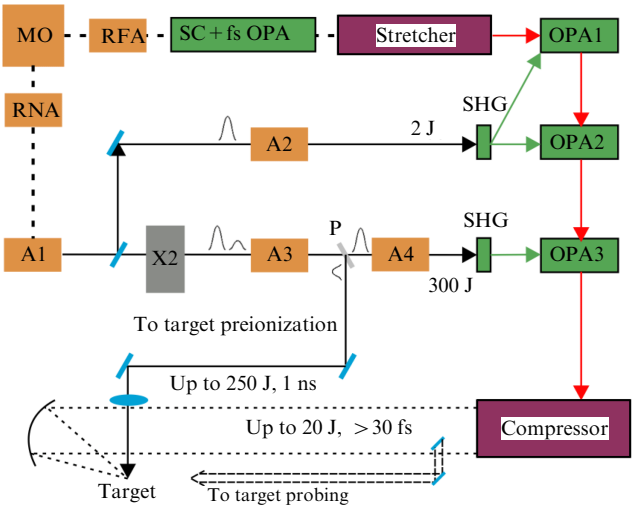

Figure 1. Schematic diagram of the PEARL laser complex with a system for nanosecond pump radiation output for target preionization. MO — master oscillator with two optically synchronized outputs, RFA and RNA — femtosecond and nanosecond regenerative amplifiers, A1–A4 — rod amplifiers, SC + fs OPA — supercontinuum generator unit with parametric amplification, OPA1–OPA3 — parametric amplifiers, SHG — second harmonic generator, X2 — two pulse formation system.

Table 1. Approximate parameters of the main operating modes of the PEARL laser complex. The parameters are sensitive to the settings of the optical setup and may significantly vary in different experimental series.

Mode	λ, nm	E, J	τ, fs	ν, Hz
Tuning	910	10^{-10}	30	70×10^6
Pulse-periodic	910	10^{-2}	30	1
Single-pulse	910	20	30	1/1200
Nanosecond	1054/527	250/180	10^6	1/1200

frequency and 180 J at the double frequency, which can potentially be used in laser–matter interaction experiments. In parametric amplification terminology, broadband radiation with a central wavelength of 910 nm will be called the signal wave or the signal, and conventionally narrowband radiation at a wavelength of 1054 nm will be called the pump. The final parametric amplification stages also contain an idler wave at a wavelength of $\sim$1250 nm, whose energy is comparable to the signal energy.

Recently, the starting section was upgraded, during which an integral starting section was installed [13], which produces optically synchronized signal and pump pulses. The upgrade has led to a dramatic reduction in jitter between the signal and the pump to sub-picosecond values and an increase in the stability of all pulse parameters, in both tuning and single-pulse modes. A schematic diagram of the laser after the update is shown in Fig. 1.

The system starts with an ytterbium fiber femtosecond master oscillator (MO) at a central wavelength of 1030 nm operating at a repetition rate of about 50 MHz. The active fiber is equipped with a piezoelectric washer that changes the length of the resonator, allowing synchronization of the source to an external clock.

2.1.1 Nanosecond pump channel. After pre-amplification in the MO fiber amplifier, a part of the femtosecond pulse is directed to the nonlinear element, where the spectrum broadens, reaching the amplification bandwidth of neodymium phosphate glass at a wavelength of 1054 nm. Using a chirped fiber Bragg grating, the spectrum of the broadened pulse is 'clipped' to a spectral band with a width of about 1 nm, stretched to a duration of about 3 ns, and sent for further amplification. The fiber amplification stage ends at an energy of about 1 μJ at a frequency of 1 kHz, after which the pulse is sequentially fed to a regenerative Yb:YLF amplifier and several diode-pumped rod amplifiers, for which the repetition rate is further thinned out to 1 Hz and the output energy reaches 2000 mJ, which provides the so-called pulse-periodic operating mode of the femtosecond system at a level of 30 mJ of the signal at 910 nm. After amplification in Yb:YLF, the signal spectrum is further narrowed to about 0.3 nm, but the signal still remains stretched with a duration of about 1 ns. The energy of the pump pulse remaining after pumping the pulse-periodic part enters a high-power flashlamp-pumped nanosecond neodymium-glass rod amplifier, where its energy increases to a level of more than 250 J [3]. When converted to the second harmonic, this pulse is used to pump the final parametric amplification stage. Recall that a pulse with a duration of about 1 ns contains linear frequency modulation within a 0.3-nm spectral interval.

The high-power amplifier is equipped with a system of division into two pulses [29], which allows increasing the efficiency of the amplifier due to more efficient extraction of population inversion from the active elements. This system can be used both to pump additional amplification stages (if they appear during further upgrades of the PEARL laser) and to generate an additional nanosecond prepulse [14] for experiments on laser-plasma interaction, while retaining the energy of the femtosecond signal.

2.1.2 Femtosecond channel. The main part of the pulse from the master oscillator MO at a wavelength of 1030 nm is amplified in a regenerative femtosecond amplifier (RFA) to a millijoule level and then sent to a system for producing femtosecond signal radiation, which operates on the basis of supercontinuum generation with subsequent parametric conversion and amplification using fs pumping (SC + fs OPA). The output pulse has a central wavelength of 910 nm, a duration of 20 fs, and an energy of about 10 μJ. The design of such a system for producing signal radiation is described in more detail in Ref. [13]. Further amplification occurs in a three-stage parametric amplifier (see Fig. 1). The first two stages are capable of operating in a pulse-periodic mode of up to 10 Hz and are pumped by a diode-pumped nanosecond pulse-periodic part. The energy in the pulse-periodic mode is $\sim$30 mJ. The final amplification stage, which is pumped by the second harmonic radiation of the nanosecond rod amplifier, increases the energy of the chirped pulse to 20 J at the compressor output. The laser repetition rate in the single-pulse mode is one shot every 20 minutes.

Due to optical synchronization and parametric frequency conversion capabilities, this architecture is very flexible and is constantly being improved. Currently, active work is underway to increase the diode-pumped fraction of the laser facility through the sequential replacement of increasingly powerful flashlamp-pumped amplifiers.

2.2 Laser beam injection into the target chamber and focusing

Both the signal pulse ($\sim$20 J, 910 nm, 30 fs) and the pump pulse ($\sim$250 J, 1054 nm, 1 ns) can be used to irradiate the target. The output intensity of the signal radiation (~ 2 TW cm^{-2}) in an aperture of $\sim$20 cm causes significant nonlinearity of the air and any pass-through optical elements, and injection into the target chamber is therefore carried out along a vacuum optical path, and focusing is performed using an off-axis parabolic mirror. The intensity of a nanosecond pulse (~ 3 GW cm^{-2}) does not require vacuumization; the pulse can be delivered to the interaction chamber through the air, passed through an optical window and focused using a lens. Potentially, idler wave radiation can also be used to irradiate the target, whose spectrum width and duration are comparable to the parameters of signal radiation. However, the use of the idler wave is associated with technical difficulties: notably, it contains angular dispersion and uncompensated negative group velocity dispersion (the sign of the chirp is different from the signal wave). Due to the latter circumstance, the idler wave cannot be compressed to a femtosecond duration [30] because of a lack of petawatt compressors with a suitable sign of the group velocity dispersion. When the target is exposed to pump radiation, in order to preserve the parameters of the signal radiation, it is most advisable to snatch the pump pulse from the final amplification stage, since in this case the pumping of the first two amplification stages does not suffer (see Fig. 1). When developing the pump amplifier of the final stage, the possibility of operating in a two-pulse mode was incorporated

[29], whereby the seed is divided into two successive pulses with orthogonal polarizations. One of the successive pulses is used to pump the final parametric OPA-3 stage (see Fig. 1), while an additional pulse can be introduced into the target chamber to irradiate the target. The setup can provide an additional pulse energy of up to hundreds of joules (250–300 J) while maintaining the signal pump parameters and, as a consequence, the femtosecond pulse.

2.3 Increasing the focal intensity of femtosecond pulses

To increase the peak intensity of a focused femtosecond pulse, two key technologies are used in the PEARL complex: wavefront correction and nonlinear post-compression.

To correct the wavefront, an adaptive optical system (AOS) is used (Fig. 2), which includes a mirror with a controlled surface shape [31] (CSM) and a wavefront sensor (WFS) located in the diagnostic channel [32], which serves to implement feedback. The diagnostic channel is conveniently located behind one of the plane mirrors of the optical path with a high reflection coefficient, where the radiation is multiply attenuated.

In the correction mode, the AOS improves the focal spot by changing the surface profile of the CSM, whose shape is controlled based on a phase conjugation algorithm [33], whose correct operation requires information about the reference wavefront shape at which the focal spot is optimal. The phase conjugation algorithm is direct and suitable for operation at high repetition rates, since it is able to compensate for rapid dynamic distortions arising, for example, from air flows in the optical path.

An imperfection of the optical elements located between the WFS and the focal spot, as well as errors in their alignment, lead to the need for an AOS calibration procedure, which consists in finding a reference wavefront shape specific to a given optical design. Calibration, in turn, is carried out by iterative methods [23, 34], which are too long to be used during routine wavefront correction. Calibration errors obviously lead to a decrease in focusing quality in the correction.

Thanks to the use of the AOS, in the single-pulse operation mode (10 J, 60 fs,one pulse every 20 minutes), it was possible to significantly improve the quality of focusing. At the initial stage in the tuning mode, the original calibration technique [23], which takes into account dynamic distortions in the optical path, made it possible to find a reference wavefront shape corresponding to the Strehl ratio (SR) of ~ 0.85. The initial focusing of the laser pulse in the single-pulse operation mode corresponded to SR = 0.26 and an RMS deviation of 0.138 μm. Furthermore, as a result of AOS operation, focusing with SR = 0.72 and an RMS deviation of 0.046 μm was achieved. Figure 3 shows the far field (a, d), wavefront shapes (b, e), as well as the near-field zones (c, f) of the beam, before (a–c) and after (d–f) correction. The corrected focal spot size at half maximum was 2.46×2.58 μm^2, which is very close to the diffraction limit of the far field distribution for an $f/2.5$ focusing. The peak intensity corresponding to such focusing would be 1.73×10^{21} W cm^{-2} for a pulse energy of 10 J and 60 fs duration.

An efficient approach to increasing the maximum power of femtosecond laser systems is the nonlinear compression technology Compression after Compressor Approach (CafCA) [21]. The technology involves spectrum enrichment in thin elements with Kerr nonlinearity with subsequent compensation of quadratic dispersion.

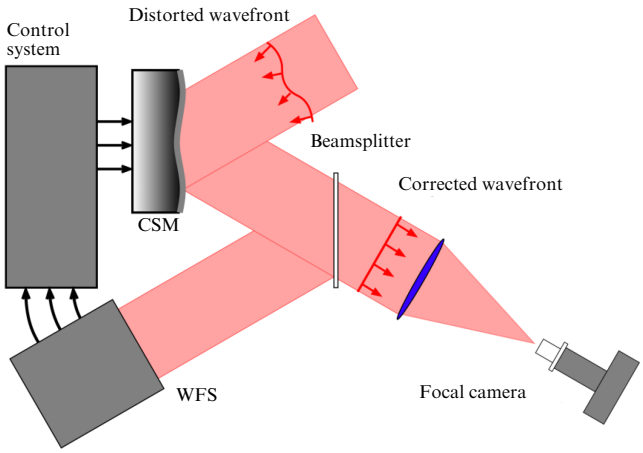

Figure 2. AOS diagram. CSM is a mirror with a controlled surface shape, PM is a flat mirror behind which the wavefront measurement channel is located, WFS is a wavefront sensor.

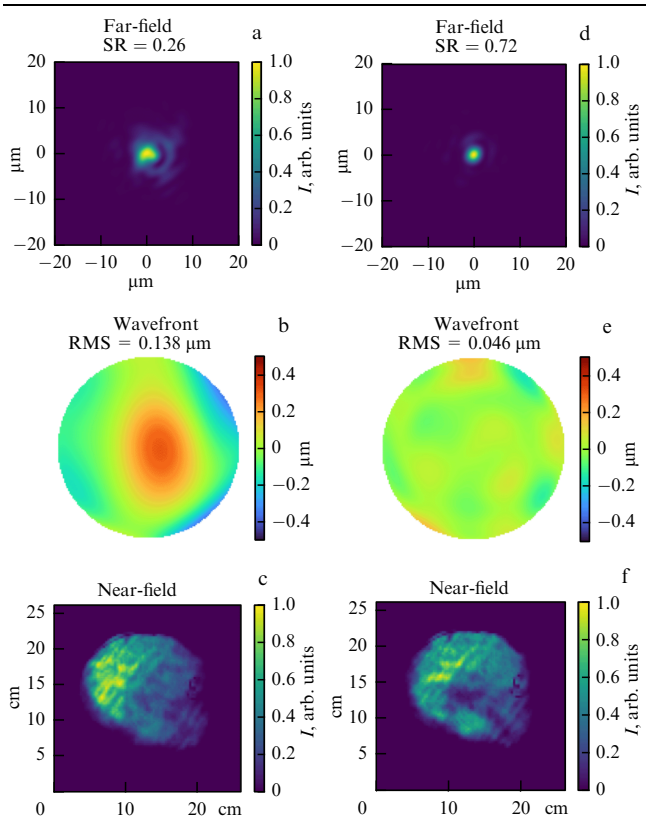

Figure 3. Far field (a, d), wavefront shape (b, e), as well as near-field (c, f) beam images before (a–c) and after (d–f) correction.

We emphasize that focusing a laser pulse after the CafCA calls for special approaches, in particular, the use of optical elements prepared to work with a broader radiation spectrum and modification of the AOS [25, 27].

Experiments on pulse focusing after the CafCA performed at the PEARL laser facility [27] suggest that the AOS allows increasing the Strehl ratio from SR = 0.15 to SR = 0.52. The results were obtained for very strong nonlinear wavefront distortions (the B-integral was equal to ~ 10) and a repetition rate of one shot every 20 minutes. The duration of a pulse compressed due to post-compression was of the order of 10 fs [26]; therefore, with a pulse energy of

10 J and an $f/2.5$ focusing system, the peak intensity in this case would be on the order of 4.73×10^{21} W cm^{-2}.

It is also worth noting that the ability to control the wavefront of a laser pulse using an AOS allows one to change the configuration of the radiation spot on the target (for example, stretch the focal spot in one direction or produce two focal spots spaced apart), as well as shift the waist plane along the optical axis within a wide range, which expands the possibilities for customizing optical setups and the range of feasible experiments.

Therefore, the ability to control the wavefront, reduce the duration of the laser pulse, and increase its peak focal intensity allows us to expand the application potential of the PEARL laser complex.

2.4 Magnetic system

In experiments with laser plasma at the PEARL facility, use is made of an original pulsed magnetic system, which makes it possible to generate pulsed (duration: ~ 5 ms) magnetic fields with an induction of up to 18 T [15]. The magnetic field is produced by a Helmholtz coil (see Fig. 4) placed in an insulated tank filled with liquid nitrogen to improve the stability of the pulse-to-pulse discharge parameters. Individual coils in the magnetic system can be connected in two ways so that the current in the coils flows in the same direction or in opposite directions. In the former case, a quasi-uniform magnetic field configuration is realized (Fig. 18a); in the latter case, a configuration with a zero magnetic field at the center, the so-called cusp configuration (Fig. 18b). Figure 18 shows the distribution of the magnetic field induction modulus for each coil configuration. The supporting housing provides the mechanical strength of the system required to withstand pulsed mechanical loads of the order of 100 MPa [15] that arise in the counter-connection. The design of the magnetic system makes it possible to observe and inject optical radiation simultaneously along several directions (see Fig. 4).

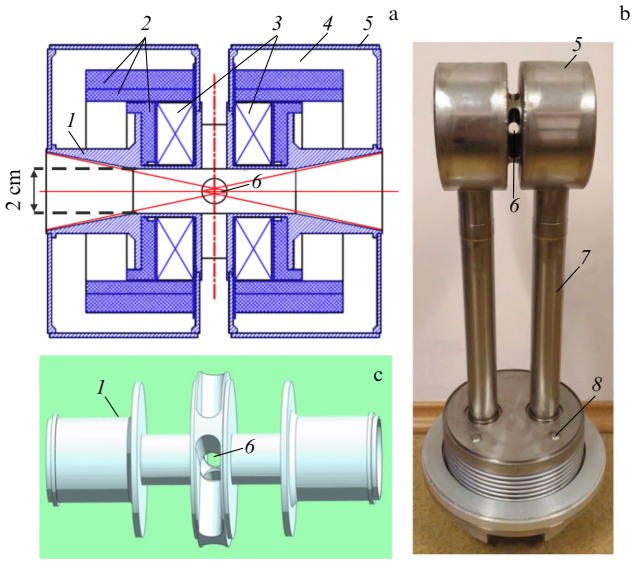

Figure 4. Schematic cross-sectional representation of the magnetic system (a), general view of the magnetic system (b), internal power part with viewing windows (c): *1* — metal power frame, *2* — composite elements of the power frame, *3* — windings, *4* — nitrogen chamber, *5* — external screen, *6* — openings for laser radiation injection and plasma flow diagnostics, *7* — nitrogen cooling channels; *8* — unit for thermal isolation and adjustment of magnetic system orientation. (Figure adapted from Ref. [15].)

2.5 Key diagnostic methods of laser-plasma interaction

Experimental research at the laboratory complex is based on a wide and permanently expanding set of techniques for diagnosing laser-plasma interactions. Some of these techniques were significantly modified for specific experimental conditions.

2.5.1 Interference diagnostics. Optical interferometry is one of the main diagnostics for visualizing laser-produced plasma in laboratory experiments [17, 35]. This diagnostic tool allows one to qualitatively study the dynamics and structure of a propagating plasma flow, identify the characteristic features of developing plasma instabilities [18, 36], and obtain quantitative estimates of the plasma propagation speed and, under certain assumptions, recover its density distribution.

A typical diagnostic scheme based on the Mach–Zehnder interferometer used in PEARL (see Section 4) is presented in Fig. 5. A low-power laser pulse with a central wavelength of 910 nm and duration < 60 fs extracted from the femtosecond channel was used as probing radiation. In different experimental campaigns, different methods were employed for extracting probing radiation from the femtosecond channel. In experiments in which a powerful femtosecond pulse was not used, the radiation from the femtosecond channel was taken entirely before the final amplification stage, compressed and directed into the target chamber through the air. In experiments using high-power femtosecond radiation, part of the laser driver was split off using a small sub-aperture mirror inserted into the main aperture at the compressor output (see Fig. 1).

Located in one of the interferometer arms in a vacuum chamber was the object under study — a plasma flow created by a high-power laser pulse. To transfer the image from the object area to the array of the recording CCD camera (C_1), use was made of a telescope consisting of two lenses, L_1 and L_2.

A delay line made it possible to vary the time of arrival of the probing pulse at the target in a range from 0 to ~ 100 ns from the instant of arrival of the pump pulse, which in a

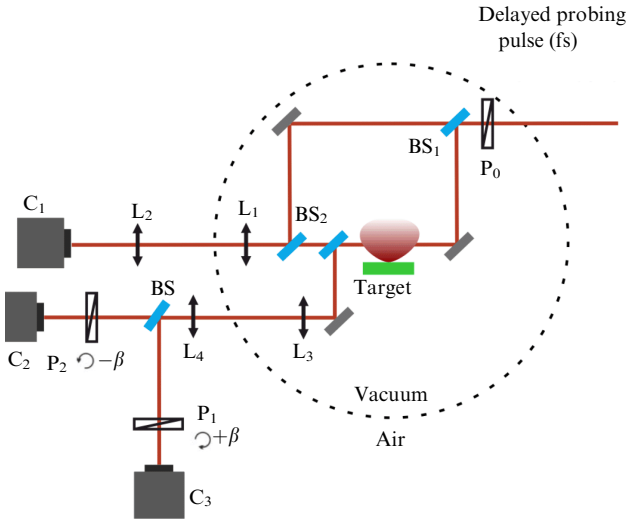

Figure 5. Schematic diagram of interference and polarimetric diagnostics.

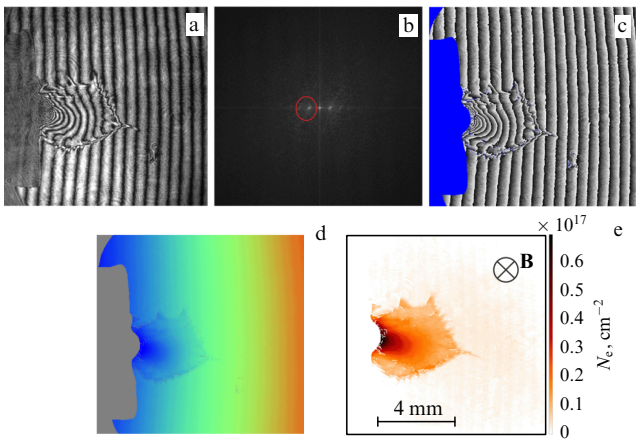

Figure 6. Main stages of interferogram processing using the IDEA software package. (a) Typical interferogram of plasma expanding into an external magnetic field (see Section 4). (b) Fourier spectrum, (c) result of Fourier filtration: a stepwise-phase image, (d) phase incursion $\phi(x, y)$ in the plasma object and the 'linear' phase (processing artifact), (e) two-dimensional linear plasma density.

number of experiments (see Section 4) was a nanosecond long.

The plasma object introduces phase distortions, which manifest themselves in the form of fringe shifts in the interference pattern relative to the unperturbed state, i.e., in the absence of a plasma object.

Figure 6 presents an example of a typical plasma flow under study and shows the main processing steps for reconstructing the two-dimensional profile of the optical radiation phase incursion $\phi(x, y)$ in the plasma from the interference pattern using the Interferometric Data Evaluation Algorithms (IDEA) package [37].

The relationship between the phase incursion along the direction of propagation of the optical pulse and the linear integral electron density N_l is uniquely defined by the formula

$$N_l(x, y) = \int_0^l N(x, y, z)\,\mathrm{d}z = \frac{2c}{\omega} N_{\mathrm{cr}} \phi(x, y)\,, \qquad (1)$$

where $N_{\mathrm{cr}} = m\omega^2/4\pi e^2$ is the critical density, ω are the frequency and wavelength of the probing pulse. The distribution profile of the linear integral density of the plasma flow is presented in Fig. 6e.

Assuming that the propagating plasma flow has cylindrical symmetry, for example, in the case of expansion along the direction of magnetic field lines [38–40], the three-dimensional plasma density can be retrieved using the inverse Abel transform proceeding from only the linear integral density profile. For an asymmetric density distribution, which arises, for example, when plasma expands across a magnetic field, several orthogonal linear integral density profiles are required to retrieve the three-dimensional plasma concentration.

For parameters characteristic of the PEARL laser facility, optical interference diagnostics make it possible to measure the density of laser-produced plasma in the range from $\sim 5 \times 10^{16}$ cm^{-3} to $\sim 10^{20}$ cm^{-3} [16–18, 36].

2.5.2 Polarimetric diagnostics. To measure the spatial distribution of magnetic fields arising in a plasma, advantage is taken of a polarimetric method based on the Faraday effect, according to which the propagation of linearly polarized optical radiation in a plasma containing a magnetic field results in a rotation of the plane of radiation polarization. From the spatial distribution of the polarization rotation angle in the probing pulse beam, one can obtain information about the distribution of magnetic fields in the plasma expanding from the target. By changing the delay of the probing pulse relative to the high-power plasma-producing pulse, the dynamics of the magnetic field is studied. A schematic diagram of polarimetric diagnostics is shown in Fig. 5.

Linear polarization of the probing radiation at the entry to the plasma is ensured by the polarizer P_0. An optical system consisting of lenses L_3 and L_4 transfers the image of the probing beam from the plasma region to the CCD cameras K_2 and K_3. After passing through the plasma region, the probe pulse is divided by the beamsplitter BS into two channels, each of which contains polarizers (P_1 and P_2). At the first stage of alignment of the diagnostic setup, pairs of polarizers P_0–P_1 and P_0–P_2 are aligned to minimize the transmittance of the probing pulse in the absence of plasma (crossed position of the polarizers). At the second stage, polarizers P_1 and P_2 are rotated relative to the crossed position by an angle β that is equal in magnitude but opposite in sign relative to the direction of propagation of the probing radiation. With this setting, rotation of the plane of polarization in the plasma leads to a decrease in the signal intensity in one of the channels and an increase in it in the other one. This setting of polarimetric channels makes it possible to find not only the amplitude but also the direction of polarization rotation [35, 41]. The polarimetric measurement configuration in use provides a spatial resolution of about 7 μm and allows one to measure the rotation of the polarization plane by angles $\geqslant 0.1^\circ$.

2.5.3 Focusing spectrometer with spatial resolution. To record the time-integrated emission spectra of laser-produced plasma in the X-ray range, FSSR (focusing spectrometer with spatial resolution) diagnostics are used in laboratory experiments [42]. Such a spectrometer has a high spectral resolution, which makes it possible to record individual characteristic atomic lines, whose intensity ratios and widths can be employed to determine the temperature and density of the plasma under study.

Figure 7 is a schematic diagram of signal recording using an FSSR.

The operation of the spectrometer is based on the spatial separation of the spectral components of plasma radiation on a spherically curved (concave) crystal. A crystal with a radius of curvature R forms an image on a circle (S_2) of radius $R/2$, that is, the beam reflected from the crystal and all diffraction orders are located on this circle.

In experiments on proton acceleration at the PEARL complex [5], use was made of a spectrometer with a characteristic spectral resolving power $\lambda/\Delta\lambda \sim 3000$ based on a spherically curved mica crystal ($2d = 19.94$ Å, where d is the interplanar distance of the crystal lattice; radius of curvature $R = 150$ mm).

The crystal tuning is specific to each specific material that makes up the target irradiated by a laser pulse. For example, in the ion acceleration experiment (see Section 3.2), the crystal was positioned in such a way as to simultaneously record the characteristic spectra of aluminum ions (He_α, K_α, and Ly_α lines) in the second order of reflection in the wavelength range of 6.8–8.43 Å (1.45–1.85 keV), as well as recombination

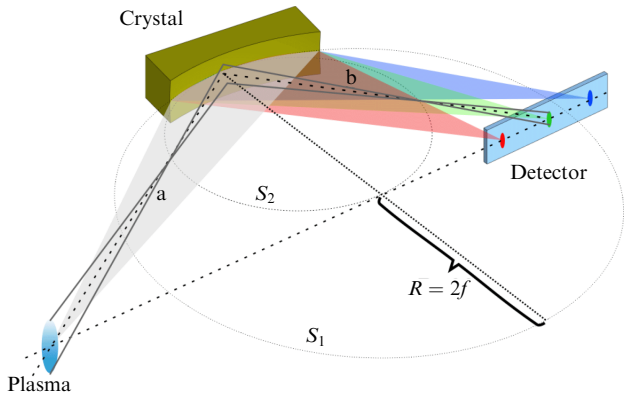

Figure 7. Signal detection setup using FSSR

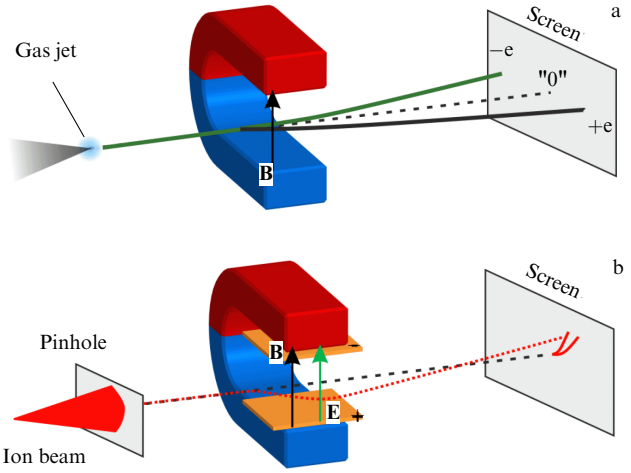

Figure 8. (a) Schematic diagram of a single-screen magnetic spectrometer. (b) Schematic diagram of the Thomson parabola spectrometer.

continuum in the energy range of 2.21–2.73 keV in the third order of reflection.

Spectra recorded using X-ray fluorescent plates (imaging plates) make it possible to estimate the plasma temperature and density in the interaction region. A typical spectrogram is shown in Section 3.2.

2.5.4 Accelerated charged particle spectrometers. To measure the spectra of charged particles, in addition to the widely used layered detectors based on radiochromic films [43] and thermoluminescent detectors [44], the PEARL complex uses special magnetic spectrometers adapted to experimental conditions.

The operation of a magnetic spectrometer is based on the dependence of the cyclotron radius of a charged particle on its kinetic energy. In the simplest case, the spectrometer consists of a magnetic system and a detector, which allows the deflection of a particle in a magnetic field to be measured (Fig. 8a).

The detector can be, for example, image plates (IP), scintillators, CCD matrices, etc. Charged particles with a higher kinetic energy are deflected to a lesser extent, which leads to blurring of the trace on the detector across the magnetic field (Fig. 9 from Section 3.1.1). Knowing the dispersion of the spectrometer, the energy spectrum of the particles can be retrieved from the trace on the detector.

Charged particle beams can have a significant angular spread, which leads to ambiguity in determining the particle emission angle when retrivering the spectrum. This can be avoided if, in the case of wide beams, a slit or a pinhole is added at some distance from the spectrometer entrance. In the case of narrow beams, a setup with two screens can be implemented [45]. Adding an additional point eliminates the ambiguity in determining the angle of particle departure and significantly reduces the error in the reconstruction of the spectrum. The angular distribution is well retrieved from the distribution of the glow along the magnetic field on the screen, that is, in the direction where the magnetic field does not deflect the particles. This has been used repeatedly in experiments at PEARL [7].

In the simplest scheme, traces on the detector left by different types of particles can overlap. When use is made of co-directed magnetic and electric fields perpendicular to the beam axis (Fig. 8b), traces from particles with different charge-mass ratios will overlap to a smaller extent and will have the shape of a parabola [46, 47]. A spectrometer with such a device is called a Thomson parabola. It allows one to observe the ion composition of a charged particle beam; the characteristic signal of the spectrometer is shown in Section 3.2.

3. Laser-plasma acceleration of charged particles

3.1 Electron acceleration

Laser-plasma acceleration by a wake field in a highly nonlinear mode (the so-called bubble regime) has been studied theoretically and experimentally for decades, but not all the features of such acceleration have been studied in detail. In one of the pioneering studies [48], conditions were proposed for a matched resonant interaction, whereby the scale of the laser pulse in the waist region conventionally coincides with the plasma wake wavelength. From Ref. [49], one can find the following relationship between the parameters of the laser pulse (w_0 is the waist diameter, a_0 is the dimensionless field amplitude) and the plasma parameters (k_p is the modulus of the wave vector of the plasma wave, R is the bubble radius): $k_p R \simeq k_p w_0 \simeq 2\sqrt{a_0}$. A similar condition is imposed on the duration of the laser pulse. If these conditions are met, the laser pulse propagates without significant changes in the pulse profile. For a matched acceleration regime, features were studied that quite accurately predict the parameters of the generated electron beams and the parameters of the laser plasma. From this theory [48], it follows that optimal acceleration conditions are achieved when the pulse length in space is equal to half the plasma wavelength, and for $f/15$ focusing and a 60-fs duration, the corresponding plasma density is 1.5×10^{18} cm^{-3}, and for $f/6$ focusing, it is higher: 5×10^{18} cm^{-3}.

However, recent experiments and numerical simulations [7, 50, 51] suggest that the energies of accelerated electrons can exceed the energies predicted for the matched regime when the parameters of the laser pulse and plasma parameters are mismatched. The mismatched regime remains largely unexplored and may be important for producing high-energy electrons. At $f/46$ focusing at a density of $\sim 1.5 \times 10^{18}$ cm^{-3}, the size of the laser pulse in the waist is 2 times the size in the matched case for such a density.

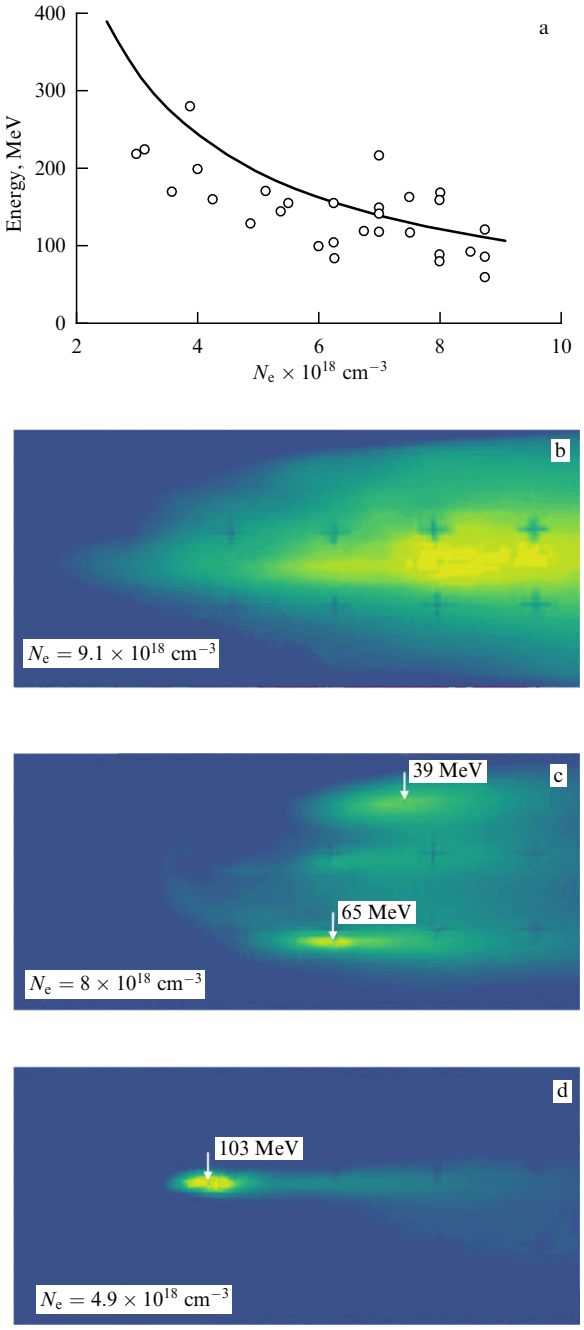

Figure 9. Density dependence of the energy of accelerated electrons (a) and electron beams at different plasma densities (b–d), corresponding to different P/P_c ratios.

Several experimental sessions were conducted at the PEARL complex aimed at studying acceleration in the wake wave in matched and mismatched modes.

3.1.1 Matched mode. The first experiment aimed at studying the acceleration of electrons in a matched mode is described in detail in Refs [6, 45]. In this experiment, whose topology is identical to that shown in Fig. 10, use was made of laser pulses with an energy of up to 10 J and a duration of 60 fs, which were focused into a gas jet by parabolic mirrors at $f/15$ and $f/6$. The gas jet was produced using a supersonic conical nozzle with diameters of 2, 5, and 10 mm, and the gas (He) supply was controlled by an electromagnetic valve. The density distribution in the jet was measured interferometrically: see Section 2.5.1. In the experiment, the density ranged from 1×10^{18} to 1.2×10^{19} cm^{-3}.

To record accelerated electrons and measure their energy, use was made of a magnetic spectrometer constructed according to a two-screen scheme [6, 45], described in Section 2.4, and suitable for measuring quasi-monoenergetic electron beams with a narrow angular distribution.

The experiment obtained monoenergetic electron beams with cutoff energies up to 300 MeV (see Fig. 9a), a minimum angular size of 6 mrad, and a charge of up to 300 pC. In this case, the highest cutoff energies corresponded to a charge of 10–20 pC and the maximum charge corresponded to an energy of 80–100 MeV. Revealed, in addition, was the dependence of the topology of electron beams on the ratio P/P_c, where P is the peak power of the laser pulse and P_c is the critical power for self-focusing. For $P/P_c < 2$, no electron beams were observed, which was apparently due to the absence of significant self-injection of electrons into the wake wave. When the threshold $P/P_c = 2$ was exceeded, single beams appeared with maximum cutoff energies, small angular size, and moderate charges. With a further increase in the P/P_c ratio, a decrease in the cutoff energy was successively observed, accompanied by an increase in the angular size of electron beams and their charges (Fig. 9d), the appearance of several beams (clustering) (Fig. 9c), and a transition to a regime with a wide angular distribution (see Fig. 9b).

3.1.2 Unmatched mode. The experimental setup [7] for laser wakefield electron acceleration in an mismatched mode is shown in Fig. 10. A high-power laser pulse at a central wavelength of 910 nm with a duration of 50–60 fs and an energy of up to 20 J was focused by an $f/46$ spherical mirror (not shown in the diagram) at the center of the target chamber, where a gas cell was located in the focal plane of the mirror. A laser pulse with a peak intensity of up to 2.3×10^{19} W cm^{-2} was focused to a spot 44 μm wide at half maximum (FWHM), ionized the gas, and excited a wake plasma wave. The length of the gas cell used in the experiment could vary in the range from 3 mm to 28 mm. The pressure of the working gas (He) at the inlet to the gas cell could vary from 0.1 to 3 bar. The ultrasonic valve was synchronized to the laser pulse and opened 30 ms before the pulse arrived.

To measure the energy spectra and angular distributions, advantage was taken of a magnetic spectrometer using a two-screen scheme (see Section 2.4) [6, 45], which was adapted to the experimental conditions. The magnetic system consisted of two round dipole magnets M_1 and M_2 (0.6 T, 6 cm in diameter) located on the axis of propagation of the laser pulse. Two scintillator screens S_1 and S_2 were used as detectors, whose glow was recorded by screens C_1 and C_2. The procedure for reconstructing the energy and angular distribution is described in detail in Ref. [7].

The main result of the experiment was the production of electron beams with maximum energies of up to 1.5 GeV. As can be seen from Fig. 11, the energies of the resulting electron beams in the range of cell lengths and gas pressure under study exceeded 150–200 MeV, while the energy of individual monoenergetic peaks in the accelerated electron spectra exceeded 500 MeV in a large fraction of shots.

The reconstructed parameters of accelerated electrons obtained in a series of experiments turn out to be in good agreement with the known dependences for the matched wake

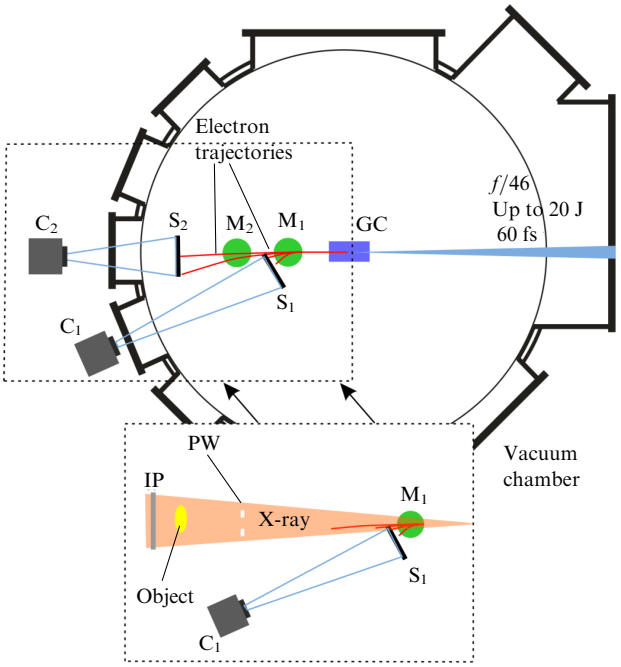

Figure 10. Layout of the experiment to study the unmatched acceleration mode: GC — gas cell; M_1, M_2 — spectrometer deflection magnets; S_1, S_2 — spectrometer scintillator screens; C_1, C_2 — CCD cameras; PW — PET window. Detail inside the marquee shows a modification of the experiment for the exposure of objects to secondary radiation (see Section 3.3.1).

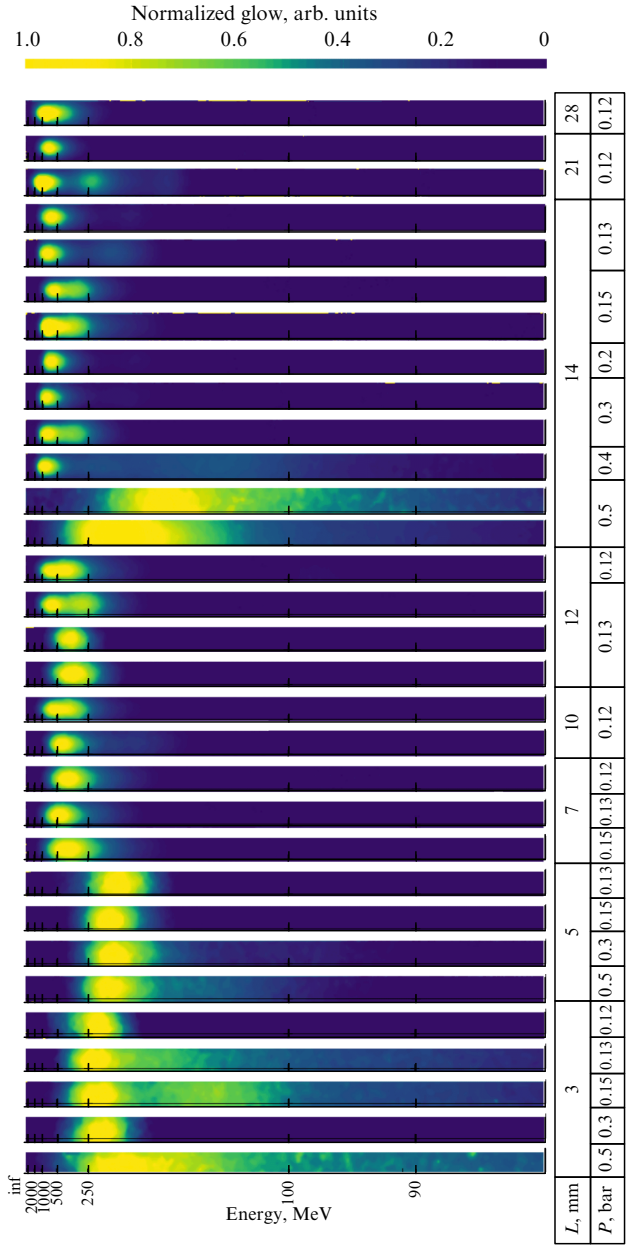

Figure 11. Selected shots of the experiment [7].

acceleration mode. In particular, for the parameters of the PEARL laser complex, there are optimal values of pressure at the gas cell inlet as well as the length of the gas cell. In the first case, the optimum is determined by the presence of two competing factors. First, an increase in pressure leads to an increase in plasma density, which results in an increase in the accelerating field. However, the energy of the optical driver begins to deplete faster, leading to a decrease in the energies of the accelerated particles. The optimum length of the gas cell, which directly affects the interaction length, corresponds to the dephasing length of the accelerated electron bunch and the wake wave.

The resultant electron beams set a record for the PEARL laser facility. The electron energies were many times higher than the values obtained in experiments in Ref. [6], during which the regimes of laser wakefield electron acceleration were chosen close to the matched bubble regime.

In Ref. [7], the gas cell density was not calibrated, but the results of numerical simulations make it possible to estimate the plasma density during interaction. In the experiment, efficient acceleration began with a valve pressure of 0.12 bar, which corresponded to a density in the numerical simulation that was 25% as high. The density assessed in this way, assuming a linear dependence of the density in the cell on the input pressure, makes it possible to estimate other parameters of the plasma. Calculating the maximum electron energies according to the matched theory, one can see (see Table 2) that the electron energies in the unmatched case exceed the theoretically possible values, which also corresponds to the results obtained by other experimental groups [50].

So, the result of the experiments on electron acceleration was the production of particles with energies up to 300 MeV in the case of matching the parameters of laser pulses with plasma parameters and up to 1.5 GeV in the mismatched mode. The record electron beams have good directivity. The results

Table 2. Parameters of electron beams and facilities at which these beams were obtained.

Facility	λ, μm	P, TW	$f/\#$	$w_0/2$, μm	N_e, 10^{18} cm^{-3}	λ_p, μm	L_{acc}, mm	ΔE_{theor}, GeV	$\Delta E_{exp,max}$, GeV
PEARL 2011 [6]	0.91	180	$f/15$	11.5	4	16.5	4	0.7	0.3
Astra Gemini [50]	0.8	215	$f/40$	31.6	2.5	20.9	16	1.2	1.6
PEARL 2020 [7]	0.91	216	$f/46$	35.2	3.6	17.4	14	0.78	1.2

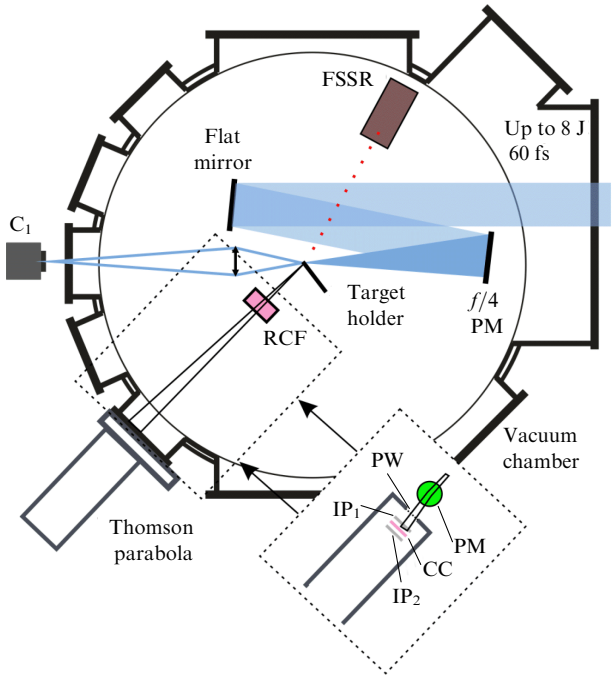

Figure 12. Schematic diagram of the experiment on ion acceleration in the TNSA regime [5]. Detail inside the marquee shows an experiment modification involving irradiation of biological objects by accelerated particles (see Section 3.3.2).

obtained are in good agreement with the well-known theory of the bubble regime and laser pulse self-trapping. An increase in the energy of accelerated particles can result in an increase in the hardness of betatron radiation, which may be used for various applications, for example, X-ray imaging (see Section 3.3.1).

3.2 Ion acceleration

The laser pulse parameters of the PEARL facility are suitable for efficient ion acceleration in the Target Normal Sheath Acceleration (TNSA) regime [52]. Despite the fact that the ion cutoff energies achieved to date (the highest energy that individual particles can acquire during acceleration) are insufficient for the implementation of socially significant applications, such as hadron cancer therapy [53], the parameters of accelerated ions obtained at leading laser facilities are well suited both for preliminary studies on the development of techniques for controlling the energy spectrum [54] and focusing [55] of an ion beam, and for proton radiography [56]. The latter is not an alternative pump-probe diagnostic in experiments with dense opaque plasma [57].

The experimental demonstration of proton acceleration took place using the setup presented in Fig. 12.

During the experimental session [5], radiation was focused with an aperture ratio of $f/4$ on the surface of aluminum foil with a thickness of 0.4 to 10 μm. The angle between the optical axis and the target surface was 45 degrees. Use was made of laser pulses with an energy of up to 10 J and a duration of about 60 fs. Wavefront correction to optimize focusing was carried out; however, the calibration of the AOS was not perfect (see Section 2.3), and residual distortions of the wavefront led to moderate values of the Strehl ratio not exceeding 0.4, which corresponded to a peak intensity of about 3×10^{20} W cm^{-2} for 10 J. The nanosecond contrast ratio is 2×10^8 and is due to enhanced parametric luminescence having the form of a pedestal, whose duration is approximately equal to the duration of the pump pulse (~ 1 ns), with the leading edge ahead of the main pulse by 0.5 ns.

To diagnose the energy spectrum of accelerated ions, two complementary diagnostic devices were used: a layered detector made of radiochromic films (RCF-stack) [43] and a Thomson parabola detector [46] (see Section 2.5.4). A hole was made in the center of the layered detector through which the accelerated particles reached the Thomson parabola, which allowed the simultaneous operation of both devices. Raw data from the spectrometers are exemplified in Fig. 13.

The electric voltage and magnetic induction in the Thomson parabola were 6.5 kV cm^{-1} and 0.4 T, respectively. Image plates (Fujifilm, model TR) in conjunction with a commercial IP scanner (HD-CR 35 DUERR NDT) were used as a detector in the Thomson parabola. The characteristic spectra of the target in the region of pulsed laser heating were analyzed using the FSSR technique (see Section 2.5.3).

Analysis of the experimental dataset confirms the high efficiency of interaction, which is apparently due to the optimal focusing and prepulse parameters, as well as the special emphasis placed on the alignment procedure. An original procedure was developed based on partial blocking of the tuning radiation by the sharp edge of the target, which is illustrated in Fig. 15. This procedure formed the basis of experiments to increase focusing sharpness by refocusing using an elliptical mirror [58] and the basis of the approach to convergence and coherent addition of beams in the XCELS project [20].

Analysis of the experimental data presented in Figs 14 and 16 indicates the efficiency of energy transfer from the laser pulse to the plasma. The cutoff energy of accelerated protons (see Fig. 13) is in the range from 43.3 MeV to 44.5 MeV, which is close to the record for the corresponding pulse energy. The highest cutoff energy was achieved for a 0.8-μm-thick target. The number of accelerated particles can be estimated from the plot in Fig. 16b. It shows the number (right scale) and energy (left scale) of particles with an energy above a certain value plotted on the horizontal axis. For example, from Fig. 16b, it could be concluded that the shot accelerated 10^7 protons with energies above 40 MeV, whose total kinetic energy was 2×10^{-4} J. The direction of fast protons coincides with the normal to the target surface and, according to Fig. 16c, higher energy particles have a narrower angular distribution, which is typical of the TNSA mode. On the Thomson parabola (Fig. 13a), in addition to the proton trace, one can see traces of carbon C^+ and oxygen O^+ ions with different charge states, which is a consequence of contamination of the rear target surface with organic compounds.

X-ray spectra (see Fig. 14a) exhibit characteristic lines and their satellites typical of the aluminum target material. The nature of the spectral intensity of the continuum radiation and the ratio of the amplitudes of the characteristic lines correspond to a temperature of about 300 eV and solid-state plasma density. Note that the spectral components located in the two ranges lying between the resonant Ly_α and He_α lines, as well as from the electronic satellites of He_α to the neutral K_α line, are due to the emission of hollow atoms KK and KL, respectively [59, 60]. Hollow atoms can only be produced in a relatively cold zone of solid density located at the periphery of the central zone and irradiated by the laser while simultaneously exposed to X-rays and fast electrons generated in the central zone. The appearance of hollow atoms indicates the presence of X-ray radiation of sufficiently high intensity

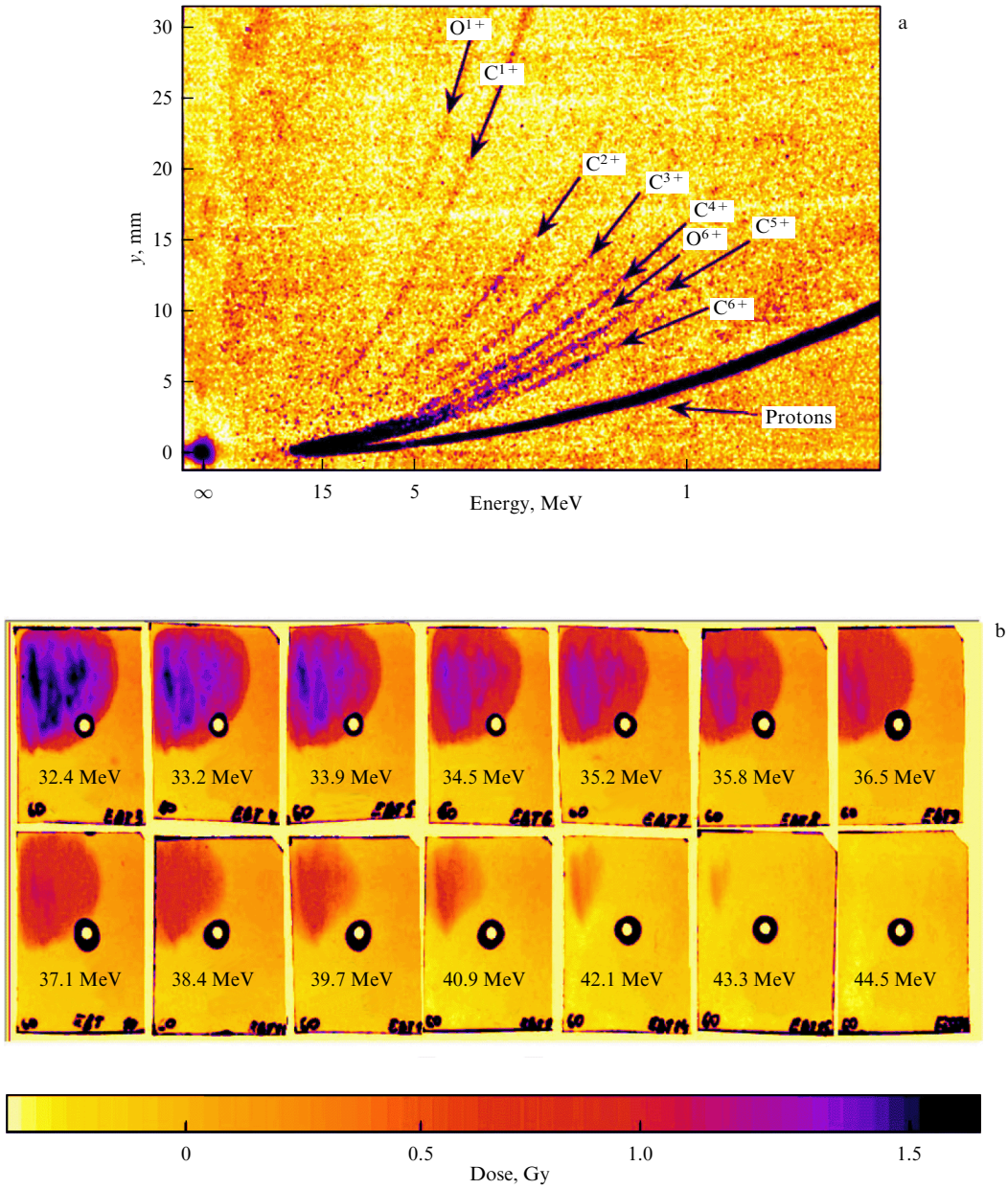

Figure 13. Spectral diagnostics of accelerated ions. Typical raw Thomson parabola data (a) and radiochromic film stack data (b) in the shot with a record cutoff energy > 43.3 MeV.

(probably exceeding 10^{17} W cm^{-2} to dominate the plasma kinetics) and of the solid-state density of the peripheral region, which is indirect confirmation of the absence of destruction of the target by the prepulse at the instant of arrival of the main pulse. X-ray radiation in this case arises through a bremsstrahlung mechanism from electrons heated by a laser pulse, which also testifies to the efficient laser-to-electrons energy transfer.

The dominant mode of energy transfer from the laser pulse to the target electrons and, as a consequence, its efficiency are determined by the spatial distribution of the plasma at the instant of arrival of the main pulse. So, the role of the prepulse in the efficiency of ion acceleration is decisive. One-dimensional numerical estimates for the moment of arrival of the main pulse suggest the presence of significant preplasma on scales of the order of 1 μm with a linear increase from 10^{21} to 10^{23} cm^{-3} [5].

So, the experimental conditions implemented at the PEARL complex in the focusing of laser radiation on thin metal foils (~ 1 μm thick) contribute to efficient ion acceleration. Proton beams have been demonstrated whose highest energy and charge are sufficient for the experimental investigation of laser-driven particle acceleration, the development of approaches to the manipulation of laser-accelerated protons using magnetic optics techniques, and the development of applications involving action on biological objects (see Section 3.3.2) and implementation of plasma field diagnostics in opaque plasmas in experiments in laboratory astrophysics and high energy density physics.

3.3 Applications of laser-driven secondary sources

As shown above, under the influence of powerful femtosecond radiation from the PEARL laser, a plasma can become a bright source of electromagnetic radiation in the X-ray range

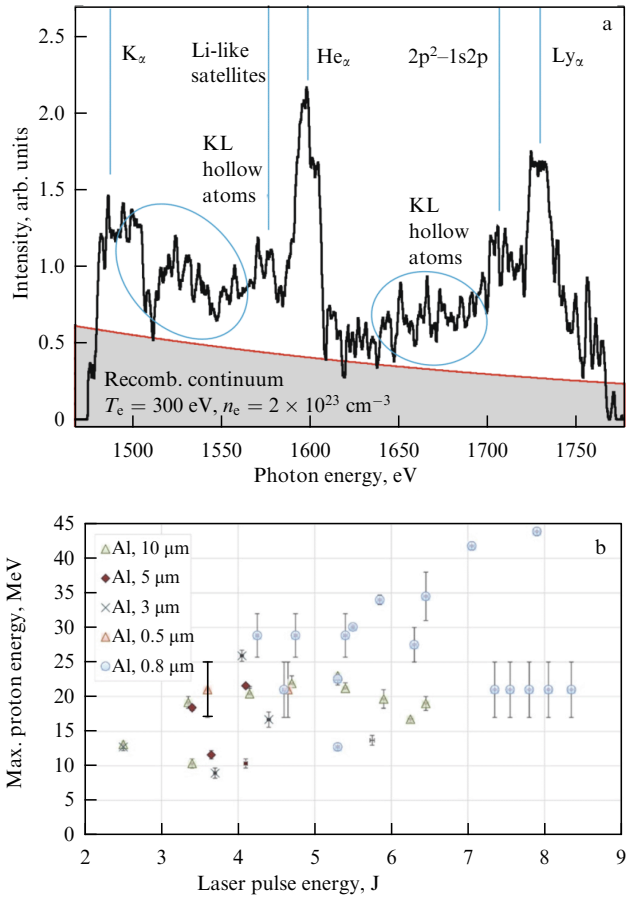

Figure 14. Results of FSSR data processing (a) and cutoff energy statistics during experimental series (b).

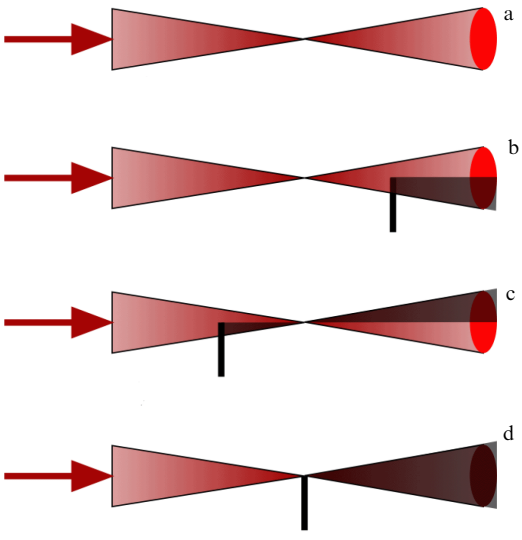

Figure 15. Diagram of alignment procedure.

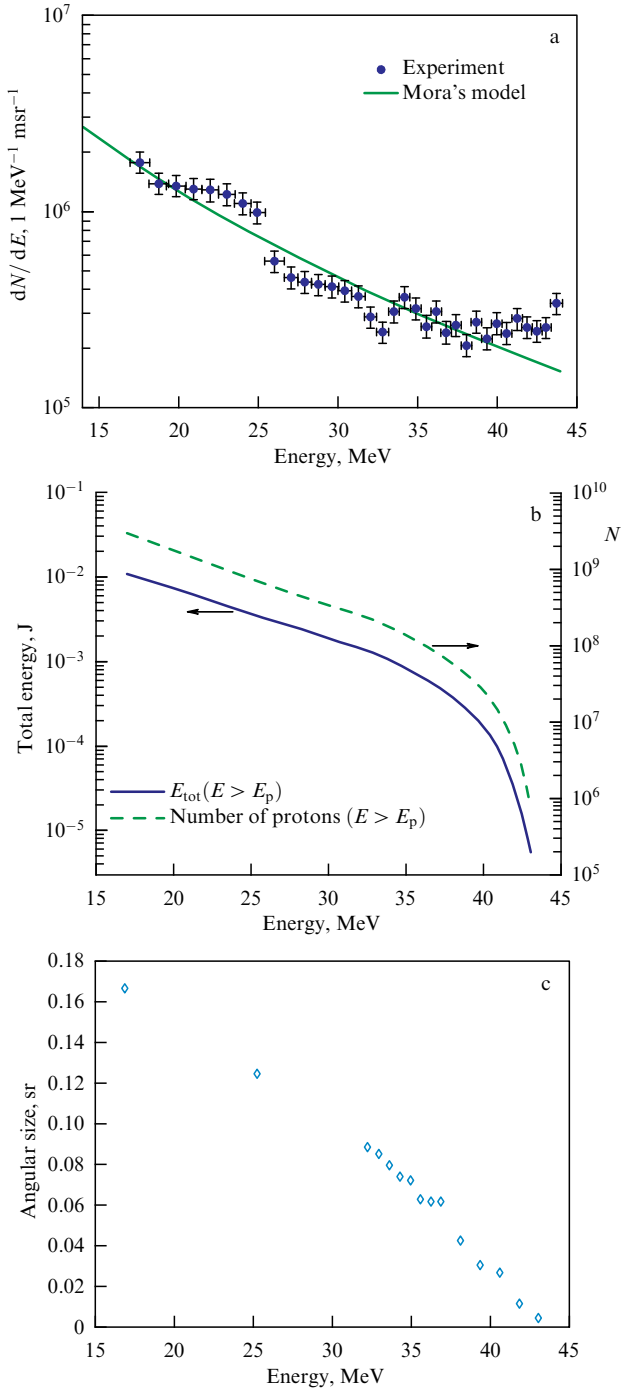

Figure 16. Spectra reconstructed from layered proton detector data: (a) energy spectrum, (b) graph characterizing the number of accelerated protons with energies above E_p and their total energy, (c) width of proton angular spectrum versus energy.

and accelerated electron and ion beams. This makes the PEARL laser-plasma complex a convenient tool for research and development of applications based on such sources of secondary radiation.

3.3.1 X-ray imaging. Inexpensive, compact, and bright X-ray sources are in demand in medicine, in particular for low-dose phase-contrast X-ray tomography for noninvasive diagnosis of tumors. Such sources of secondary radiation can be obtained in the highly nonlinear mode of interaction of a relativistically intense laser pulse with plasma. Electrons accelerated in a plasma wave undergo transverse betatron oscillations, resulting in the generation of electromagnetic radiation. For typical laser pulse-plasma interaction parameters, the frequency of betatron radiation is in the X-ray region of the electromagnetic spectrum [61].

Based on the experimental technique for laser-wakefield electron acceleration using a gas cell, which was described in

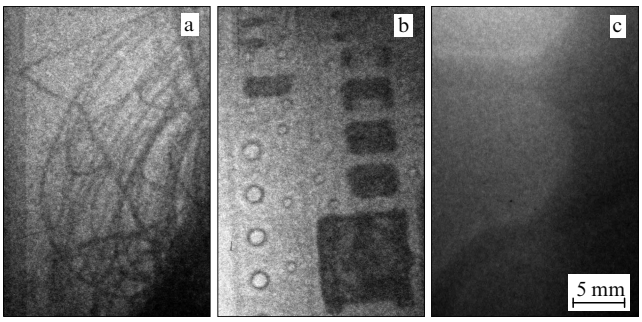

Figure 17. Typical images of objects irradiated by betatron X-ray radiation: (a) coil of wire, (b) microcircuit, (c) paw and tail of a laboratory mouse.

detail in Section 3.1 and in Ref. [7], a series of experiments were performed aimed at using betatron X-ray radiation for imaging optically opaque objects.

The experimental setup is schematized in Fig. 10. A laser pulse (wavelength: 910 nm; duration: 60 fs; energy: up to 20 J) was focused onto the input pinhole of a gas cell (GC) with helium (pressure at the valve inlet: up to 5 atm). To measure the energy spectra of accelerated electrons, one magnetic spectrometer was used consisting of a permanent magnet magnetic system (M_1) and a scintillator screen (S_1); the emitted radiation in the optical range was recorded by a CCD camera (C_1) with an optical lens. Located on the optical axis of the laser radiation, outside the volume of the target chamber, was an object irradiated by the generated betatron X-ray radiation. X-ray images were taken using an image plate (IP) placed behind the object. To minimize the influence of absorbing materials on the generated betatron radiation, a 0.2-mm-thick window (LW) made of PET $(C_{10}H_8O_4)_n$ was used at the output flange of the target chamber, which was located on the axis of laser radiation.

Figure 17 shows X-ray images of different objects: a metal wire (a), a microcircuit (b), and parts of a paw and the tail of a laboratory mouse (c). The relatively low contrast of the resultant images may be associated with parasitic illumination of the detector by the bremsstrahlung of accelerated electrons interacting with elements of the circuit and target chamber or with nonoptimal plasma parameters, leading to fragmentation of the laser pulse into multiple filaments and, as a consequence, to an increase in the effective size of the source. There is every reason to expect that blocking parasitic light sources and optimizing plasma parameters will raise the quality of the resultant images to the level typical of such facilities [62, 63].

3.3.2 Proton therapy. Compact sources of laser-accelerated protons are of interest for medical applications, primarily in terms of cancer therapy. The existence of a Bragg absorption peak in ions [64], whose depth depends on the kinetic energy of the proton upon entering living tissue, makes it possible to localize the effect on the irradiated tumor and reduce the radiation load on surrounding healthy tissue. Currently, laser-plasma ion acceleration technologies do not provide the ion beam parameters required for widespread use in medicine. In particular, the record experimentally achieved cutoff energy values of about 94 MeV [65] are lower than the level of $\sim$250 MeV required for proton therapy [66]. However, the potential advantages of therapy, such as low cost and compactness, make work on the development of these technologies highly relevant. Development of basic techniques for laser-accelerated proton delivery and their effect on biological subjects is already possible using existing laboratory complexes [67, 68].

To test methods for the influence of laser-accelerated protons on biological subjects, the setup used in experiments on proton acceleration (see Section 3.2) was supplemented with a module for placing living subjects and equipment for ensuring the vital activity of living cell cultures [69]. The module was a metal cylinder 0.5 m long, mounted in one of the flanges of the target chamber, allowing the substrate with cells to be placed at a minimum distance of 0.3 m from the source of laser-accelerated protons.

Figure 12 is a schematic diagram of the experiment. A laser pulse (wavelength: 910 nm; energy: 10 J; duration: 60 fs) was focused in the target chamber onto a 10-μm-thick aluminum target mounted at an angle of 45° to the incident radiation. The energy spectrum of a proton beam laser-accelerated in the TNSA mode was measured using a stack of radiochromic films (RCF) located at a distance of 35 mm from the target normal to its surface. The typical cutoff energy of the proton spectrum was on the order of 20 MeV. The stack had a hole 3.5 mm in diameter through which a proton beam was delivered from the vacuum volume through a 0.1-mm-thick, 15-mm-diameter plastic window (PW) onto a substrate with a cell culture (CC) located at atmospheric pressure. The parameters of the proton beam traveling onto the substrate were estimated based on the dose received by the stack films in the region adjacent to the hole; in this case, since the characteristic angular size of the proton beam in experiments usually significantly exceeded the size of the hole in films for energies less than 20 MeV, the angular distribution inside the hole was considered homogeneous. A system of permanent magnets (PMs) with a diameter of 6 cm and an induction of 0.4 T was used for energy separation of the proton beam, which made it possible to differentiate the effects of proton and X-ray irradiation on the cells. To control the dose of radiation deposited in the cell culture, image plates (IP_1 and IP_2) were placed on the front and back sides of the substrate. In this geometry, doses in the area where the cell culture was located reached tens of Grays. The study subject was a human cervical cancer cell culture (HeLa Kyoto [70]), which is a common model for biological research due to the active growth and ease of maintaining this type of cell in laboratory conditions. One day before irradiation with a proton beam, the cells were cultured in Dulbecco's Modified Eagle Medium (DMEM). Since the proton beam exited the target in a horizontal plane, immediately before the instant of a shot, the nutrient medium was removed and the substrate was placed vertically in the biomodule. After irradiation of the cells, a fresh nutrient medium was added, and the plate was placed in a CO_2 incubator for a day. Then, an MTT assay was performed to assess the proportion of cells that survived the experiment.

The experimental study suggests that biological tissues can receive integral radiation doses of tens of Grays as a result of a single shot, sufficient to cause damage and even significantly exceeding the doses required for therapeutic purposes. However, since the energy spectrum of accelerated protons was not monoenergetic, which is critical for proton therapy, the action was not local. The experiment implemented the simplest method of energy separation using permanent magnets. However, due to the magnetic field being insufficiently strong for the given experiment geometry, the separation in energy

was weakly pronounced. An additional negative factor in using this separation technique is a significant reduction in the dose received by the study subject, and, consequently, the need to accumulate the radiation dose required on the irradiated subject over a large number of shots. The separation system can be improved using magnetic optics techniques to additionally focus the proton beam with retention of separation efficiency, for example, by using a 'chicane' [71] or a more complex system of permanent magnets [72].

4. Laboratory astrophysics

Laboratory astrophysics is an auxiliary method of astrophysical research, which provides the capability to simulate the dynamics of cosmic plasma under the controlled conditions of a laboratory experiment.

High-power lasers capable of creating hot dense plasmas have become a convenient tool for laboratory modeling of a broad range of astrophysical phenomena [16, 18, 39, 73–78], including studies of shock waves and post-shock turbulence in supernova explosions, hydrodynamic instabilities in an accretion disk and clouds of supernova remnants, studies of magnetic reconnection in stellar flares and coronal ejections, and modeling astrophysical jets in young stars, quasars, and galactic nuclei. Of particular interest are extreme astrophysical objects containing nonequilibrium plasma or producing strong magnetic fields responsible for the dynamics, acceleration, and radiation of particles [79].

Research in the field of laboratory astrophysics was also carried out at the PEARL laser complex. The required experimental conditions were produced in the interaction of femtosecond or nanosecond laser radiation with solid targets, whose ionization produced a high-density plasma expanding at a supersonic speed of the order of 100–500 km s^{-1}.

The plasma produced in the target irradiation by a nanosecond pulse has an electron distribution function (EDF) close to equilibrium. The dynamics of such a plasma can be described with good accuracy using hydrodynamic or magnetohydrodynamic (MHD) approaches. A femtosecond pulse produces a plasma with a nonequilibrium EDF, in which a high-energy anisotropic electronic component stands out. The behavior of nanosecond and femtosecond laser plasmas in the laboratory differs significantly, in particular, in the nature of the instabilities that arise.

The scale of experimental laser plasma is several and tens of millimeters, which is significantly smaller than astrophysical scales; characteristic times in the laboratory, amounting to tens of nanoseconds, are also many orders of magnitude shorter than the typical astrophysical ones. The equivalence of laboratory and astrophysical systems is achieved by satisfying similarity or scaling criteria.

The approach used for the scalability of laboratory nanosecond and astrophysical plasmas is based on the Euler similarity, described in detail in the work of Ryutov [78, 80–82]. For the case of ideal magnetic hydrodynamics, systems with similar topology evolve in a similar way in the coincidence of the similarity parameters: $\mathrm{Eu} = V(\rho/p)^{1/2}$ — the Euler number — and the plasma beta coefficient $\beta = 8\pi p/B^2$, where V is the flow velocity, ρ is the mass density, $p = k_\mathrm{B}(n_\mathrm{i}T_\mathrm{i} + n_\mathrm{e}T_\mathrm{e})$ is the thermal pressure (k_B is the Boltzmann constant, $n_{\mathrm{i,e}}$ and $T_{\mathrm{i,e}}$ are the densities and temperatures of ions and electrons, respectively), and B is the magnetic induction. Euler's similarity is applicable only within the framework of ideal MHD equations, when dissipative processes that can affect the hydrodynamics can be ignored. To ignore dissipative terms, it is necessary that the following parameters be much greater than unity: Reynolds number Re (the ratio of the inertial force to viscosity force), which is responsible for viscous dissipation; magnetic Reynolds number $\mathrm{Re_m}$ (the ratio of magnetic convection to magnetic diffusion), responsible for diffusion associated with finite conductivity; Peclet number Pe (the relationship between convective and molecular heat transfer mechanisms) [80].

For the case of femtosecond plasma, in which kinetic effects are important, the use of one scaling or another becomes a more complex issue, specific to concrete experimental conditions.

4.1 Investigation of kinetic instabilities in laser plasma

In a plasma with an anisotropic velocity distribution of charged particles, Weibel instability can arise [19]. Any noise perturbation of the magnetic field in this case leads to pinching or filamentation of electrons along the 'hottest' direction, which in turn will lead to an enhancement of the noise magnetic field. Small-scale magnetic fields that arise in such plasma objects due to instability development significantly affect the subsequent dynamics of particles and the macroscopic dynamics of the plasma as a whole. Weibel instability occurs in the nonequilibrium plasma of the coronal arcs of stars of late spectral classes, in the solar corona, and in the magnetospheric plasma of exoplanets. Weibel instability can be observed in experiments and numerical simulations in the irradiation of a solid target by high-power femtosecond laser pulses [83–85]. In this case, the dynamics of development and scale of Weibel instability are determined by the nonequilibrium fraction of hot electrons.

The model experiment at the PEARL facility involved irradiating a target made of polymethyl methacrylate (plexiglass) with a high-power femtosecond driving laser pulse with an energy of up to 10 J and a duration of no longer than 60 fs. The laser radiation intensity at the target ranged up to 1.5×10^{18} W cm^{-2}. The target was placed in a quasi-uniform magnetic field with an induction of up to 18 T produced by a pulsed magnetic system (see Section 2.4). The target was located along the magnetic field lines (Fig. 18a). As a result of ablation of a solid target by a pumping pulse, a plasma flow was produced, which expanded at a speed of about 100 km s^{-1} perpendicular to the target surface and magnetic field lines.

The dynamics of the laser plasma were studied interferometrically (see Section 2.5.1) in two mutually perpendicular directions (see Fig. 18a) and using polarimetric diagnostics (see Fig. 19 and Section 2.5.2) at time intervals from zero to hundreds of nanoseconds after the arrival of the laser driver.

Shown in Fig. 20 are plasma images obtained approximately 8 ns after target irradiation. The top row corresponds to a shot with an energy of 7.6 J and no magnetic field. The bottom row corresponds to a shot with an energy of 4.4 J and with an external magnetic field with an amplitude of 17.3 T turned on. Figures 20a and d show interferograms obtained using probe beam *3* (see Fig. 18a). Figures 20b and e show interferograms, and Fig. 20c and f show pictures of the two-dimensional distribution of the depolarization angle obtained using probe beam *2* (Fig. 18a).

Observed in the images (Fig. 20b, c, e, f) is the filamentation of femtosecond laser plasma in the direction across the target surface. The diameter of individual filaments was

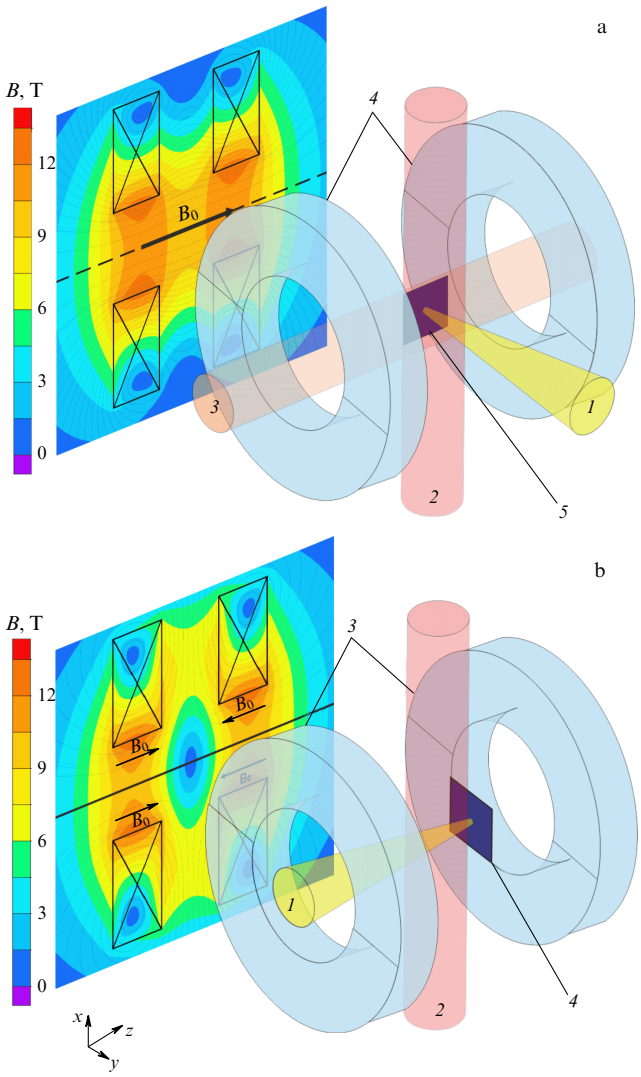

Figure 18. Principal topology of experiments and corresponding magnetic field distributions with parallel (a) and serial (b) connection of the coils of the magnetic system. Field maps located in figures on the left reflect structure of magnetic field at the center of the coil in the region of laser-plasma interaction.

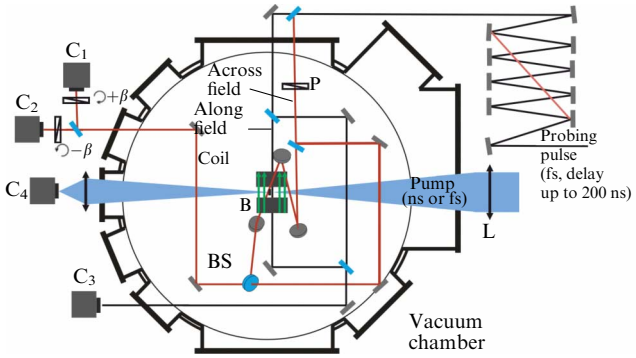

Figure 19. Basic general scheme of experiments. C_2, C_3 — CCD cameras of interferometers, C_1, C_2 — CCD cameras for polarimetric diagnostics, BS — beamsplitter, P — polarizer, L — lens.

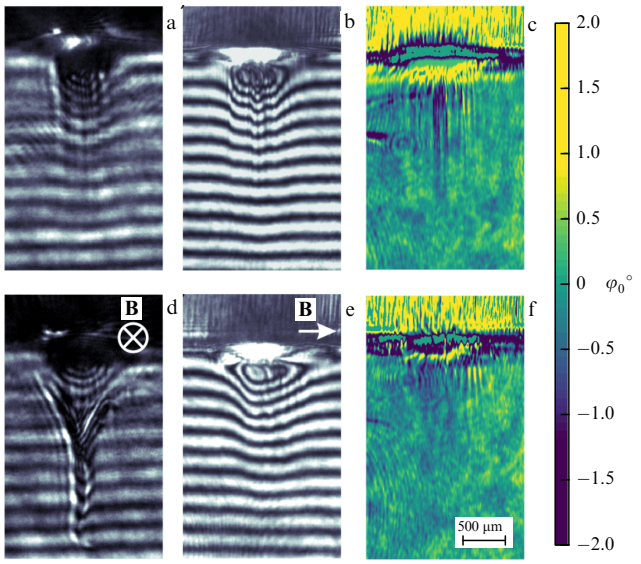

Figure 20. Experimental plasma images obtained 8.2 ns after target irradiation in shots with parameters $E = 7.6$ J, $B = 0$ T (top row) and $E = 4.4$ J, $B = 17.3$ T (bottom row). (a, d) — interferograms obtained in diagnostic channel with probing beam *3* (Fig. 18a), (b, e) — interferograms obtained in diagnostic channel with probing beam *2* (Fig. 18a). (c, f) — distribution of depolarization angle obtained in same channel *2*.

approximately 10 μm, and the spatial period of their arrangement was 30 μm. In this case, the expansion of the plasma is anisotropic: even in the absence of a magnetic field, a rather narrowly directed flow is formed, with an opening angle of the order of several degrees, along the normal to the target. This is significantly different from nanosecond ablation (see the next paragraph 4.2) and may be due to the presence of a hot electron fraction. The appearance of filaments in the plasma was observed starting from a minimum probe pulse delay time of about 0.5 ns. A rather unexpected result from the standpoint of Weibel instability theory is that the filamentation persists for quite a long time, up to 15 ns. The characteristic value of the rotation angle of the plane of polarization in the filament regions (Figs 20c and f) was of the order of $\phi \approx 0.5-1°$. In this case, the magnetic field, taking into account the electron density obtained from interferometric measurements, is estimated at the level of $B = 0.5-1$ MG.

The engagement of an external magnetic field parallel to the target surface noticeably affects the dynamics of the femtosecond plasma. Within 4 ns after the arrival of the laser driver, the influence of the magnetic field is insignificant. This is apparently determined by the fact that the plasma pressure noticeably exceeds the pressure produced by the magnetic field. Later, however, when the plasma density becomes lower, the magnetic field begins to significantly change the plasma structure (compare Figs 20a and 20d). In a plane orthogonal to the magnetic field, the plasma is strongly compressed by magnetic pressure (Fig. 20d), and a plasma sheet is formed, which over time continues to propagate from the target perpendicular to the magnetic field at a speed of the order of $V \approx 100$ km s^{-1}. Filaments are no longer observed in this sheet (see Figs 20d and f).

So, in the plasma expanding from the surface of a solid target produced by high-intensity femtosecond laser radiation, filament formation is observed, which is accompanied by the generation of magnetic fields at the megagaus level. The experimental results apparently indicate that the Weibel instability at the essentially nonlinear stage maintains a strong magnetic field, which leads to the expulsion of plasma

from the region occupied by the field, and, accordingly, to an increase in plasma concentration inside the current filaments. The magnetic field applied along the target surface leads to the formation of a plasma sheet propagating at a speed of $V \approx 100$ km s^{-1} from the target surface across the magnetic field. In the plasma sheet itself, no filament formation is observed.

Grounded assumptions about the cause for the persistence of plasma filamentation and small-scale magnetic field at such long times call for additional theoretical and numerical analysis. Full-fledged large-scale three-dimensional numerical calculations that would simulate plasma dynamics and instabilities down to a few nanoseconds have not been performed, so a comparison of numerical calculations with experiments is not yet available. The absence of such calculations is primarily due to the considerable complexity of numerical PIC simulations.

4.2 Nanosecond laser plasma

Used most often for laboratory modeling of processes in astrophysical objects are nanosecond laser systems like the PEARL pump laser [16–18, 38, 86]. For example, laboratory research on processes such as supernova explosions, the formation and emission of galactic jets, the accretion of matter onto black holes and young stellar objects, magnetic reconnection in the Sun, and solar flares are conducted using nanosecond lasers [73, 74].

4.2.1 Laboratory modeling of accretion in young stars. Accretion is the process of increasing the mass of an object due to the capture of external matter. The accretion process is typical of many types of astrophysical objects, from protostars early in their evolution to galactic nuclei. The main subjects of modeling in the work carried out at PEARL have been protostars absorbing matter from the surrounding accretion disk, in some regions of which the Eulerian similarity with laser plasma flows is fulfilled with high accuracy.

The energy release, hence the luminosity, of the star, as well as the generation of axisymmetric outflows (jets) directly depends on accretion. Therefore, studies of accretion mechanisms are crucial for understanding the evolution of stars. The interaction of the magnetosphere of a protostar with the accretion disk gives rise to complex configurations of magnetic fields and plasma flows. Observations do not allow us to determine the exact accretion scenario, and therefore laboratory experiments that model these processes are of special value.

In the literature, the most popular model is that of accretion in the form of funnel flows, in which accretion flows follow the magnetic fields of the star and fall onto the surface of the star at high latitudes. However, this type of accretion from a homogeneous disk cannot explain the observed variations in the luminosity of some types of protostars [87]. For example, irregular and strong bursts of luminosity are observed in rather exotic and poorly studied protostars such as EXor and FUor [88]. These bursts are associated with intermittent and high-energy events of magnetospheric accretion, whose cause, however, is still not clear. It is hypothesized that such accretion can be caused by a strong local disturbance of the edge of the accretion disk associated, for example, with the influence of external objects, stars [89], and giant planets [90, 91], as well as with the thermal instability of the disk [92] and magnetic activity of the star

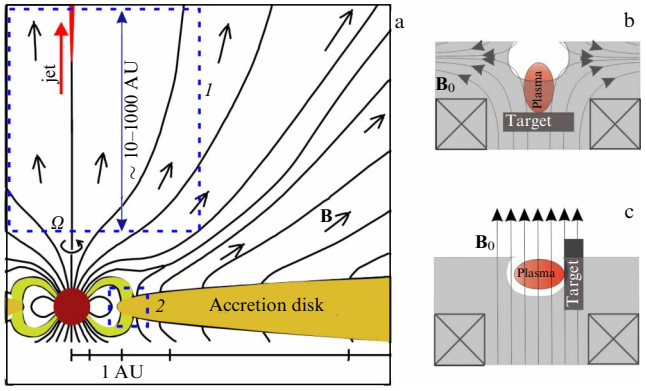

Figure 21. Diagram showing regions modeled in the experiment: *1* — jet formation region, *2* — region of matter accretion onto a young star. Corresponding experiment topologies are presented in the right column: *1* — cusp geometry with coils connected in series, *2* — quasi-uniform field with coils connected in parallel.

[93]. However, these hypotheses focus on perturbation mechanisms and do not specify the accretion process. In Ref. [16], abstracting from the mechanism of disk perturbation and assuming that a local perturbation has already occurred, the accretion process itself was investigated. The study was aimed at examining the possibility of a plasma flow propagating across the external magnetic field in the vicinity of the equatorial plane, or whether plasma flows can move only along the external magnetic field and collide with stars at high latitudes.

In the model experiment, the local perturbation of the accretion disk was simulated by plasma produced in the ablation of a solid target by a nanosecond pulse from the PEARL pump laser with an energy of the order of 10–15 J (see Fig. 21c). The magnetosphere was simulated by a uniform transverse 13.5 T magnetic field, as shown in Fig. 21c.

A schematic diagram of the experiment is given in Fig. 18a and coincides with the diagram given in Section 4.1, which was used to investigate kinetic instabilities in femtosecond laser plasma. The plasma expansion was recorded by interferometric and polarimetric diagnostics (Fig. 19), described earlier in Sections 2.5.1 and 2.5.2. The radiation intensity on the target was varied from 3×10^{10} W cm^{-2} to 3×10^{13} W cm^{-2} due to changes in the diameter of the laser spot on the target when the lens L was shifted along the direction of the nanosecond pulse.

Target irradiation produced plasma with a large pressure gradient directed perpendicular to the target surface. As a result, the plasma flow accelerated up to speeds of the order of 500 km s^{-1}. Figure 22 shows two-dimensional profiles of the linear density of the plasma flow in two projections. At the initial stage, immediately after target irradiation, the hot plasma pressure far exceeds the magnetic pressure, and therefore the shape of the flow does not differ from the flow expanding into the vacuum, i.e., a quasi-isotropic conical shape with an opening angle of about 40° (not shown in Fig. 22). As a result of the expansion of the plasma and its interaction with the magnetic field, the pressures are equalized and a diamagnetic cavity is formed (see Figs 6 and 22a), on the boundary of which there is a region of compression of the magnetic field. The spatial size of the cavity is perfectly described by the so-called stopping radius, which in the CGS

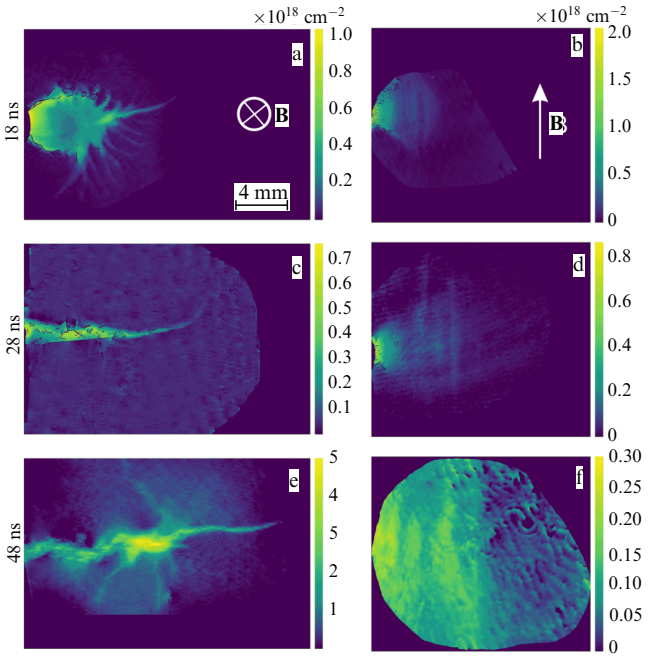

Figure 22. Experimental distributions of the linear density of laser plasma flow 18 ns (a, b), 28 ns (c, d), and 48 ns (e, f) after laser irradiation of the target. Pictures on the left are for probing along the magnetic field, and on the right, for probing across.

is expressed as

$$R_b = \left(\frac{6E}{B_0^2}\right)^{1/3}$$

[94, 95], where E is the energy deposited in the plasma and B_0 is the external magnetic field. At the same stages, the Rayleigh–Taylor instability begins to develop at the cavity boundary, as can be seen in Fig. 22a. At further stages, the cavity collapses and the plasma flow is compressed along the y-axis (Figs 22c and e). Since the movement of plasma along the magnetic field (x-axis) is not limited in any way, the flow gradually transforms into a plasma sheet (Figs 22b, d, f).

So, it was demonstrated in a model laboratory experiment that the plasma flow associated with a local perturbation of the edge of the accretion disk can penetrate across the magnetic field of the magnetosphere. Numerical MHD simulations in Ref. [36] indicate that the observed uniform propagation of plasma sheets across the magnetic field is associated with Hall effects (Hall fields and currents). It is worth saying that similar experiments were carried out at other facilities, for example KI1, but on completely different plasma scales ($R_b \sim 1$ m), which stems from the use of much more moderate magnetic fields of ~ 0.1 T. This approach made it possible to measure Hall fields and currents using probe diagnostics [96] and confirm the mechanism of plasma sheet penetration into a magnetic field.

However, the accretion mechanism of a homogeneous accretion disk, more typical of classical T Tauri stars (CTTSs), may vary greatly. Three-dimensional numerical MHD simulations of the accretion of matter onto such a star from a homogeneous disk [87] suggest two main accretion scenarios. In the first version, accretion occurs in funnel-shaped flows following the magnetic field lines (see Fig. 21a) [97–99], which collide with the surface of the star in the polar regions. In the second case, long thin 'tongues' of plasma, which result from Rayleigh–Taylor (RT) instability develop-

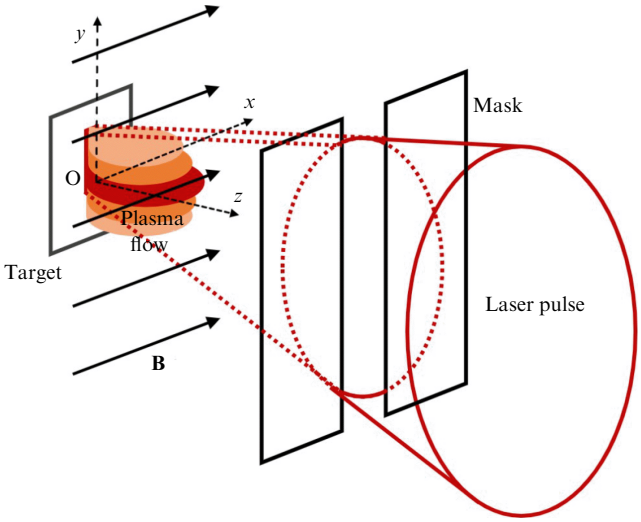

Figure 23. Schematic representation of accretion disk simulation experiment. Rectangular-shaped laser beam propagates along the z-axis and is focused on the target surface located in the yz plane; 13.5-T magnetic field is oriented along the x-axis. Figure borrowed from Ref. [18].

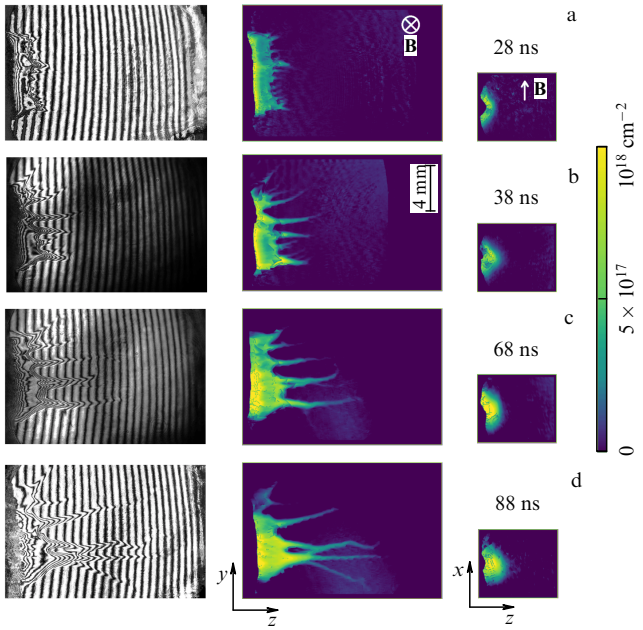

Figure 24. Two-dimensional electron density profiles of propagating plasma flow in the yz plane (a, c, e, g) and xz plane (b, d, f, h) 28 ns (a), 38 ns (b), 68 ns (c), and 88 ns (d) after laser irradiation of the target. Spatial scale shown in (c) is the same for all images. Figure borrowed from Ref. [18].

ment, penetrate into the stellar magnetosphere in the equatorial plane (see Fig. 21a).

Outlined below are the results of modeling of a uniform accretion disk interacting with the stellar magnetosphere, which were published in Ref. [18]. To simulate the geometry of interaction of a uniform accretion disk with the stellar magnetic field, a plasma flow was produced whose linear size along the y coordinate was 10 times greater than the size along the x coordinate [18] (Fig. 23). To produce such a flow, a mask in the form of a rectangular aperture with a gap of 10 mm was placed in the path of the laser pulse (Fig. 23), which provided a quasi-rectangular spot 1 mm × 10 mm in size with an intensity of about 3×10^{10} W cm^{-2} on the target surface (Fig. 23).

Figure 24 shows the experimental results, two-dimensional pictures of the integral density of the plasma flow. As

a result of interaction with an external transverse uniform magnetic field of induction of 13.5 T, the flow breaks up into separate sub-flows, so-called tongues (see Figs 24a – d). In the *yz* plane (Fig. 24a), one can clearly see that the development of instability, which divides the plasma flow into several subflows, or so-called tongues, occurs already at an early stage (prior to 28 ns) and close to the target surface. In the projection onto the *xz* plane (Fig. 24, right), no specific structure is observed, which means that in the three-dimensional form each tongue is a plasma sheet elongated in the *xz* plane but compressed by the magnetic field in the *yz* plane. After flow division into tongues, it turns out that their propagation occurs at approximately a constant speed (100 km s^{-1} for the most developed tongue). In Ref. [18], a detailed analysis of the instability was performed, and it was shown that the most plausible explanation for the expanding plasma decay into observable tongues is the development of Rayleigh–Taylor instability.

Summarizing the result on the last two points, we emphasize that the hydrodynamics of a femtosecond plasma flow (produced by a high-power femtosecond laser pulse) differ markedly from the dynamics of a nanosecond flow (produced by a nanosecond pulse). First, unlike nanosecond plasma, the femtosecond plasma does not exhibit a stage with the formation of a plasma cavity, that is, when the hydrodynamic pressure of the flow is balanced by magnetic pressure. Second, the development of Rayleigh–Taylor instability is not observed. In this case, the energies of the drivers and the magnitudes of the applied magnetic fields coincide. These differences can be attributed to the difference in absorbed energy between femtosecond and nanosecond ablation.

4.2.2 Laboratory modeling of jet collimation in young stars. Jets are supersonic, narrowly directed axisymmetric outflows that are most often observed in accreting stellar objects. It is believed that the phenomenon of jets is directly related to star formation, since it is precisely the jets that are assumed to be responsible for the removal of angular momentum from the accretion disk [100].

At the moment, there is no consensus in the scientific community regarding the mechanisms that underlie the collimation of protostellar outflows into jets. There are many theoretical models of collimation, which quite often contradict each other (see Refs [101–109]). A rather promising model is collimation by a uniform poloidal magnetic field, proposed in numerical study [109] and subsequently demonstrated in a laboratory experiment [38, 77, 110, 111].

However, the actual structure of the large-scale magnetic field near protostars (at scales of the order of 100 AU from the star) differs significantly from the idealized picture of a uniform poloidal magnetic field [112–117] and has an hourglass morphology compressed by the accretion disk in the direction of the protostar (shown schematically in Fig. 21a).

A laboratory study of the possibility of jet collimation in a highly nonuniform magnetic field with an hourglass structure (cusp structure) was carried out using the PEARL laser complex. The dynamics of the laser plasma flow in the previously studied case of a uniform magnetic field [38, 77, 110, 111] were compared with the case of strongly diverging magnetic lines. Here, special attention was paid to the evolution of the plasma when passing through a region with a zero magnetic field, located at the center of the magnetic

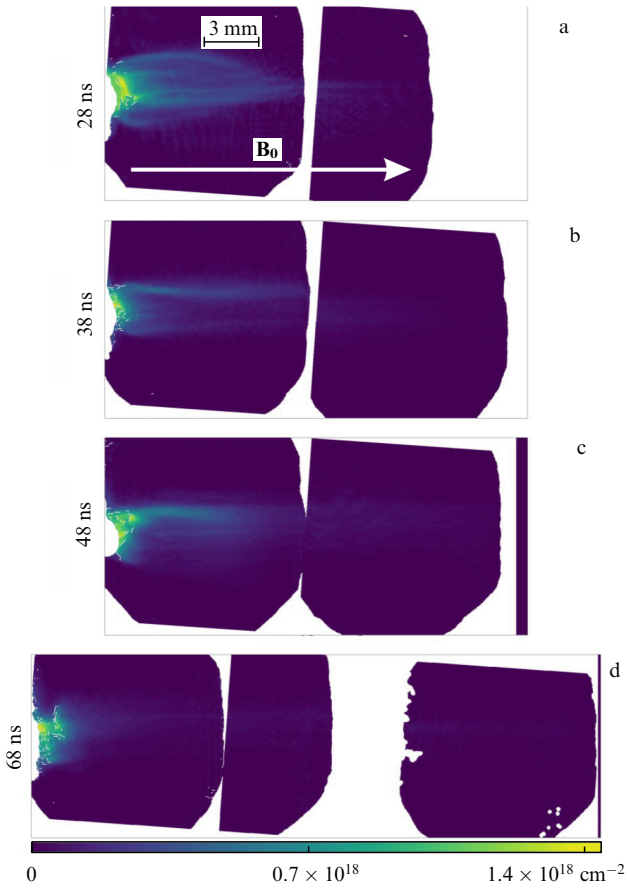

Figure 25. Profiles of the linear density of plasma flow propagating along a quasi-uniform magnetic field at points in time 28 ns (a), 38 ns (b), 48 ns (c), and 68 ns (d) after arrival of the laser driver. Spatial scale shown in (a) is the same for all figures. To increase observed area, each panel is assembled from several experimental images corresponding to different positions of the target relative to the clearance of the magnetic system.

structure. The experiment was performed according to an experimental setup similar to that shown in Fig. 19. The topology of the relative arrangement of the magnetic field and the target and diagnostic channels is shown in Fig. 18b. The plasma expansion was recorded interferometrically (see Section 2.5.1).

Experimental data (Fig. 25) suggest that the evolution of the plasma flow in a uniform poloidal magnetic field goes through several stages. The initially diverging plasma flow is supermagnetosonic and is therefore capable of deforming magnetic field lines. At the stage when the dynamic pressure of the plasma becomes equal to the magnetic pressure, the plasma flow is redirected to the axis along the magnetic field and a plasma cavity is formed (Fig. 25a). At the top of the cavity, a conical shock wave is formed, which is called a magnetic nozzle [39, 118] and which collimates the flow into a narrow jet (Fig. 25b, c).

In the cusp configuration (see Fig. 26), the dynamics of the plasma flow were studied in relation to the distance from the source to the zero point. As expected, when the target was located in the immediate vicinity of the null region, the magnetic field had hardly any effect on the plasma dynamics, and the observed flow pattern was similar to expansion without a magnetic field, which is a quasi-uniform diverging conical plasma flow with an opening angle of about 40° (Fig. 26a). However, even a small target displacement to a

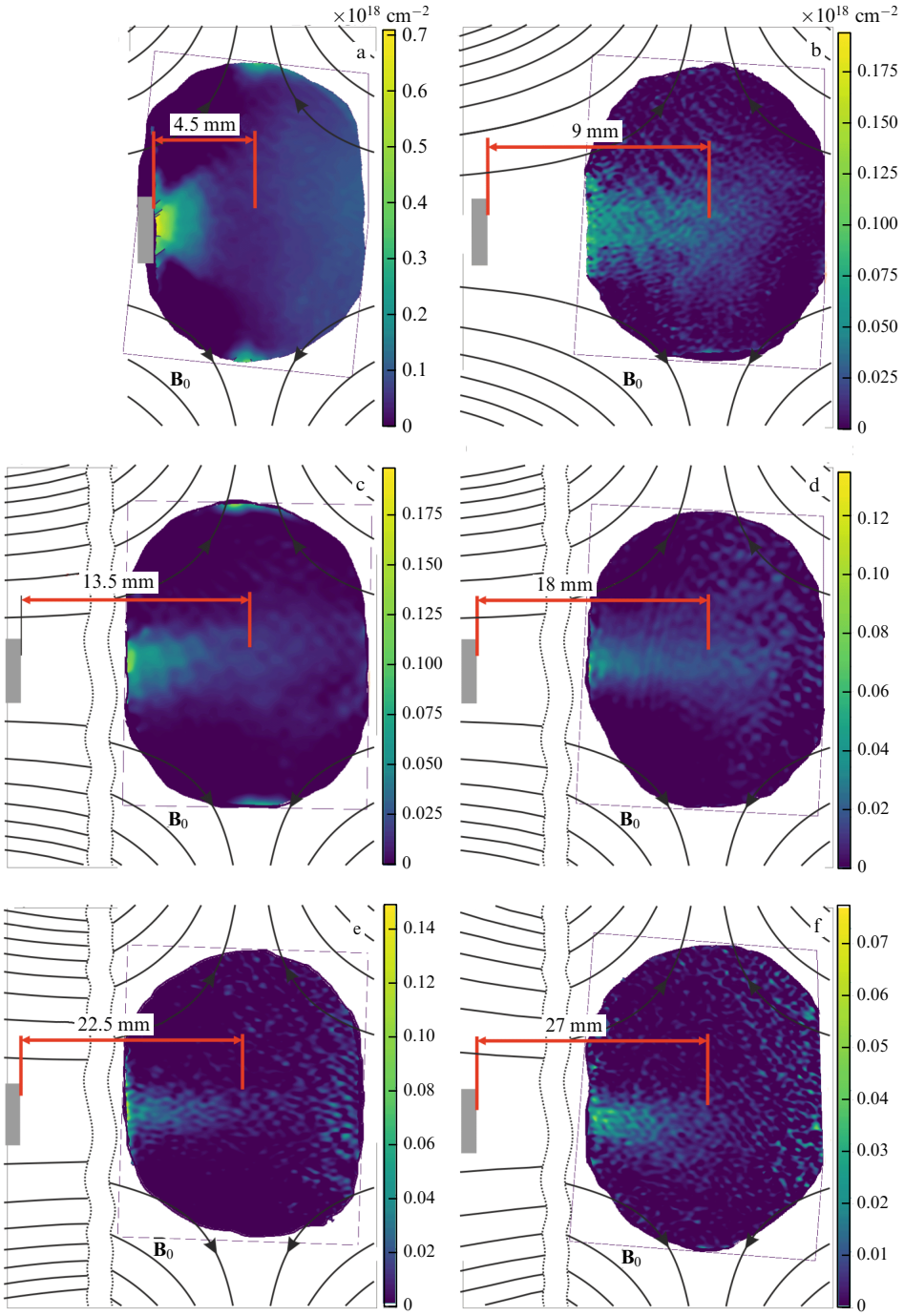

Figure 26. Linear density profiles of plasma flows propagating through the region of a zero magnetic field for different target positions. Interferometric measurements are carried out 68 ns after the arrival of the laser driver. Gray rectangle indicates target location. Results (c–f) are presented with spatial discontinuity.

position located at a distance of $2R_b = 9$ mm from the zero point (Fig. 26b) entails a noticeable narrowing of the flow. Further displacement of the target inside one of the magnetic coils at a distance of 13.5 mm or more from the center of the magnetic system leads to the formation of well-collimated plasma flows propagating through the zero region (Fig. 26c–f).

So, it was shown that a relatively small ($\sim 2R_b$) domain of a uniform poloidal magnetic field is sufficient for the formation of a jet, and further ballistic propagation of the jet can occur (see Fig. 26c–f) even in diverging magnetic field lines and in the crossing of zero points. These conclusions, considering the similarity of laboratory and astrophysical processes, expand our understanding of the mechanisms of astrophysical jet formation.

The uniqueness of the research performed is due to the technical difficulties of producing highly nonuniform magnetic fields at the level of 10 T. The need for such a high magnetic field is due to scaling in the simulation, in which one of the conditions is the coincidence of the Alfven Mach number M_A in the laboratory and astrophysical cases (for more details, see Refs [16, 78, 119]). It became possible to generate such a magnetic field thanks to the unique enhanced

magnetic system used in the experiments at PEARL (for more details, see Section 2.4 and Ref. [15]).

5. Conclusions

The experimental activities at the PEARL laser-plasma complex based on a petawatt laser have been overviewed. The available experimental potential, including the capabilities for sharp focusing of femtosecond laser pulses and nonlinear post-compression power enhancement (CafCA) have been analyzed. The key diagnostic techniques, in particular, interferometric and polarimetric diagnostics, X-ray spectrometry with focusing spectrometer spatial-resolution (FSSR) and magnetic charged particle spectrometers have been described. The results of the experiments performed on the PEARL laser facility in the main areas of research, including laser-plasma acceleration of charged particles, applications of laser-driven secondary sources, and laboratory astrophysics have been presented.

The experiments performed at the PEARL complex are not limited to those described in this review. Many of the results obtained are in the course of processing and comprehension. These include experiments on direct laser-driven electron acceleration when irradiating of porous targets of near-critical density, a feasibility study for increasing the maximum energy of laser protons by refocusing the laser driver by an elliptically shaped plasma mirror with an increase in numerical aperture, experiments in the Raman amplification of laser pulses in plasma, etc. The analysis of the data obtained on the acceleration of electrons and protons at grazing incidence of femtosecond pulses on the surface of smooth and serrated solid targets is currently at the final stage.

The PEARL laboratory complex is a unique platform for Russia, allowing a wide range of research in the field of laser-plasma interaction physics. The results of the experiments presented in the review demonstrate the possibility of carrying out research at the complex that is not inferior to that performed at similar laser-plasma complexes around the world.

Acknowledgments. The results presented in Section 2 were obtained within the framework of the Program for Setting-up and Developing a World-Class Scientific Center, Photonics Center, with financial support from the Ministry of Science and Higher Education of the Russian Federation, agreement no. 075-15-2022-316. Research in the field of charged particle acceleration and plasma physics was carried out within the framework of the scientific program of the National Center for Physics and Mathematics (High Energy Density Physics Project. Stage 2023–2025). Applications of secondary radiation sources were studied with the support of the Ministry of Science and Higher Education of the Russian Federation within the framework of the Federal Scientific and Technical Program for the Development of Synchrotron and Neutron Research and Research Infrastructure for 2019-2027, agreement no. 075-15-2021-1361.

References

1. Lozhkarev V V et al. *Laser Phys. Lett.* **4** 421 (2007)
2. Katin E V et al. *Quantum Electron.* **33** 836 (2003); *Kvantovaya Elektron.* **33** 836 (2003)
3. Poteomkin A K et al. *IEEE J. Quantum Electron.* **45** 854 (2009)
4. Bredikhin V I et al. *J. Cryst. Growth* **259** 309 (2003)
5. Soloviev A et al. *Sci. Rep.* **7** 12144 (2017)
6. Soloviev A A et al. *Nucl. Instrum. Meth. Phys. Res. A* **653** 35 (2011)
7. Perevalov S E et al. *Plasma Phys. Control. Fusion* **62** 094004 (2020)
8. Danson C N et al. *High Power Laser Sci. Eng.* **7** e54 (2019)
9. Kiriyama H et al. *Crystals* **10** 783 (2020)
10. Hong W et al. *Matter Radiat. Extremes* **6** 064401 (2021)
11. Burdonov K et al. *Matter Radiat. Extremes* **6** 064402 (2021)
12. Mukhin I B et al. *Quantum Electron.* **51** 759 (2021); *Kvantovaya Elektron.* **51** 759 (2021)
13. Mukhin I B et al. *Appl. Opt.* **62** 2554 (2023)
14. Andreev N E et al. *Quantum Electron.* **51** 1019 (2021); *Kvantovaya Elektron.* **51** 1019 (2021)
15. Luchinin A G et al. *Rev. Sci. Instrum.* **92** 123506 (2021)
16. Burdonov K et al. *Astron. Astrophys.* **648** A81 (2021)
17. Soloviev A A et al. *Radiophys. Quantum Electron.* **63** 876 (2021); *Izv. Vysh. Uchebn. Zaved. Radiofiz.* **63** 973 (2020)
18. Burdonov K et al. *Astron. Astrophys.* **657** A112 (2022)
19. Weibel E S *Phys. Rev. Lett.* **2** 83 (1959)
20. Kostyukov I Yu et al. *Bull. Lebedev Phys. Inst.* **50** (Suppl. 6) S635 (2023); *Kvantovaya Elektron.* **51** 95 (2023)
21. Khazanov E et al. *High Power Laser Sci. Eng.* **11** e78 (2023)
22. Khazanov E A, Mironov S Yu, Mourou G *Phys. Usp.* **62** 1096 (2019); *Usp. Fiz. Nauk* **189** 1173 (2019)
23. Kotov A V et al. *Quantum Electron.* **51** 593 (2021); *Kvantovaya Elektron.* **51** 593 (2021)
24. Soloviev A A et al. *Quantum Electron.* **50** 1115 (2020); *Kvantovaya Elektron.* **50** 1115 (2020)
25. Martyanov M et al. *J. Opt. Soc. Am. B* **39** 1936 (2022)
26. Ginzburg V et al. *Opt. Express* **29** 28297 (2021)
27. Soloviev A et al. *Opt. Express* **30** 40584 (2022)
28. Kotov A V et al. *JINST* **17** P07035 (2022)
29. Shaykin A A et al. *Quantum Electron.* **46** 371 (2016); *Kvantovaya Elektron.* **46** 371 (2016)
30. Yakovlev I V *Quantum Electron.* **44** 393 (2014); *Kvantovaya Elektron.* **44** 393 (2014)
31. Samarkin V V et al. *Quantum Electron.* **45** 1086 (2015); *Kvantovaya Elektron.* **45** 1086 (2015)
32. Aleksandrov A G et al. *Quantum Electron.* **40** 321 (2010); *Kvantovaya Elektron.* **40** 321 (2010)
33. Kudryashov A V et al. *Proc. SPIE* **4270** 37 (2001)
34. Sheldakova J V, Rukosuev A L, Kudryashov A V *Proc. SPIE* **5333** 106 (2004)
35. Basov N G et al. *Diagnostika Plotnoi Plazmy* (Dense Plasma Diagnostics) (Moscow: Nauka, 1989)
36. Khiar B et al. *Phys. Rev. Lett.* **123** 205001 (2019)
37. Hipp M et al. *Proc. SPIE* **3745** 281 (1999)
38. Albertazzi B et al. *Science* **346** 325 (2014)
39. Higginson D P et al. *High Energy Density Phys.* **23** 48 (2017)
40. Revet G et al. *Sci. Adv.* **3** e1700982 (2017)
41. Flacco A et al. *Nat. Phys.* **11** 409 (2015)
42. Faenov A Ya et al. *Phys. Scr.* **50** 333 (1994)
43. Bolton P R et al. *Phys. Med. Eur. J. Med. Phys.* **30** 255 (2014)
44. Horst F et al. *Nucl. Instrum. Meth. Phys. Res. A* **782** 69 (2015)
45. Soloviev A A et al. *Rev. Sci. Instrum.* **82** 043304 (2011)
46. Thomson J J *Proc. R. Soc. Lond. A* **89** 1 (1913) https://doi.org/10.1098/rspa.1913.0057
47. Rhee M J *Rev. Sci. Instrum.* **55** 1229 (1984)
48. Pukhov A, Meyer-ter-Vehn J *Appl. Phys. B* **74** 355 (2002)
49. Lu W et al. *Phys. Rev. ST Accel. Beams* **10** 061301 (2007)
50. Poder K, PhD Thesis (London: Imperial College, 2017) https://doi.org/10.25560/56216
51. Sahai A A *IEEE Trans. Plasma Sci.* **47** 2847 (2019)
52. Daido H, Nishiuchi M, Pirozhkov A S *Rep. Prog. Phys.* **75** 056401 (2012)
53. Ledingham K W et al. *Appl. Sci.* **4** 402 (2014)
54. Chen S N et al. *Rev. Sci. Instrum.* **85** 043504 (2014)
55. Nishiuchi M et al. *Appl. Phys. Lett.* **94** 061107 (2009)
56. Cobble J A et al. *J. Appl. Phys.* **92** 1775 (2002)
57. Kugland N L et al. *Rev. Sci. Instrum.* **83** 101301 (2012)
58. Kumar D et al. *Matter Radiat. Extremes* **4** 024402 (2019)
59. Skobelev I Yu et al. *Phys. Usp.* **55** 47 (2012); *Usp. Fiz. Nauk* **182** 49 (2012)
60. Faenov A Ya et al. *Sci. Rep.* **5** 13436 (2015)

61. Kneip S et al. *Nat. Phys.* **6** 980 (2010)
62. Fourmaux S et al. *Opt. Lett.* **36** 2426 (2011)
63. Wenz J et al. *Nat. Commun.* **6** 7568 (2015)
64. Bragg W H, Kleeman R *London Edinburgh Dublin Philos. Mag. J. Sci.* **10** 318 (1905)
65. Higginson A et al. *Nat. Commun.* **9** 724 (2018)
66. Mohan R, Grosshans D *Adv. Drug Delivery Rev.* **109** 26 (2017)
67. Kraft S D et al. *New J. Phys.* **12** 085003 (2010)
68. Zeil K et al. *Appl. Phys. B* **110** 437 (2013)
69. Burdonov K F et al. *Quantum Electron.* **46** 283 (2016); *Kvantovaya Elektron.* **46** 283 (2016)
70. Gey G O, Coffman W D, Kubicek M T *Cancer Res.* **12** 264 (1952)
71. Chen S N et al. *Rev. Sci. Instrum.* **85** 043504 (2014)
72. Nishiuchi M et al. *Appl. Phys. Lett.* **94** 061107 (2009)
73. Remington B A et al. *Phys. Plasmas* **7** 1641 (2000)
74. Remington B A, Drake R P, Ryutov D D *Rev. Mod. Phys.* **78** 755 (2006)
75. Kuranz C C et al. *Astrophys. Space Sci.* **336** 207 (2011)
76. Zweibel E G, Yamada M *Annu. Rev. Astron. Astrophys.* **47** 291 (2009)
77. Revet G et al. *Nat. Commun.* **12** 762 (2021)
78. Ryutov D D *Phys. Plasmas* **25** 100501 (2018)
79. Uzdensky D A, Rightley S *Rep. Prog. Phys.* **77** 036902 (2014)
80. Ryutov D et al. *Astrophys. J.* **518** 821 (1999)
81. Ryutov D D, Drake R P, Remington B A *Astrophys. J. Suppl.* **127** 465 (2000)
82. Ryutov D D et al. *Phys. Plasmas* **8** 1804 (2001)
83. Garasev M A et al. *J. Plasma Phys.* **88** 175880301 (2022)
84. Zhou S et al. *Phys. Rev. Lett.* **121** 255002 (2018)
85. Quinn K et al. *Phys. Rev. Lett.* **108** 135001 (2012)
86. Fazzini A et al. *Astron. Astrophys.* **665** A87 (2022)
87. Kulkarni A K, Romanova M M *Mon. Not. R. Astron. Soc.* **386** 673 (2008)
88. Audard M et al., in *Protostars and Planets VI* (The University of Arizona Space Science Series, Eds H Beuther et al.) (Tucson, AZ: The Univ. of Arizona Press, 2014) p. 387
89. Bonnell I, Bastien P *Astrophys. J. Lett.* **401** L31 (1992)
90. Lodato G, Clarke C J *Mon. Not. R. Astron. Soc.* **353** 841 (2004)
91. Nayakshin S, Lodato G *Mon. Not. R. Astron. Soc.* **426** 70 (2012)
92. Bell K, Lin D N C *Astrophys. J.* **427** 987 (1994); astro-ph/9312015
93. Armitage P J *Astrophys. J. Lett.* **833** L15 (2016)
94. Zakharov Yu P et al. *Plasma Phys. Rep.* **32** 183 (2006); *Fiz. Plazmy* **32** 207 (2006)
95. Winske D et al. *Front. Astron. Space Sci.* **5** 51 (2019)
96. Berezutsky A G et al. *Plasma Phys. Rep.* **49** 351 (2023)
97. Romanova M M et al. *Astrophys. J.* **595** 1009 (2003)
98. Romanova M M et al. *Astrophys. J.* **578** 420 (2002)
99. Koenigl A *Astrophys. J. Lett.* **370** L39 (1991)
100. Königl A, Salmeron R, Wardle M *Mon. Not. R. Astron. Soc.* **401** 479 (2010)
101. Ferreira J, Dougados C, Cabrit S *Astron. Astrophys.* **453** 785 (2006)
102. Blandford R D, Payne D G *Mon. Not. R. Astron. Soc.* **199** 883 (1982)
103. Matt S, Pudritz R E *Astrophys. J.* **632** L135 (2005)
104. Goodson A P, Böhm K-H, Winglee R M *Astrophys. J.* **524** 142 (1999)
105. Ferreira J, Pelletier G, Appl S *Mon. Not. R. Astron. Soc.* **312** 387 (2000)
106. Ferreira J *Astron. Astrophys.* **319** 340 (1997)
107. Shu F et al. *Astrophys. J.* **429** 781 (1994)
108. Spruit H C, Foglizzo T, Stehle R *Mon. Not. R. Astron. Soc.* **288** 333 (1997)
109. Matt S, Winglee R, Böhm K-H *Mon. Not. R. Astron. Soc.* **345** 660 (2003)
110. Higginson D P et al. *High Energy Density Phys.* **23** 48 (2017)
111. Korobkov S V et al. *Astron. Rep.* **67** 93 (2023); *Astron. Zh.* **100** 107 (2023)
112. Schleuning D A *Astrophys. J.* **493** 811 (1998)
113. Girart J M, Crutcher R M, Rao R *Astrophys. J.* **525** L109 (1999)
114. Lai S-P et al. *Astrophys. J.* **566** 925 (2002)
115. Girart J M, Rao R, Marrone D P *Science* **313** 812 (2006)
116. Kwon W et al. *Astrophys. J.* **879** 25 (2019)
117. Hull C L H et al. *Astrophys. J.* **892** 152 (2020)
118. Ciardi A et al. *Phys. Rev. Lett.* **110** 025002 (2013)
119. Zemskov R et al. *Astron. Astrophys.* **681** A37 (2024)